Reports on Progress in **Physics**



REPORT ON PROGRESS • OPEN ACCESS

Recent developments in tornado theory and observations

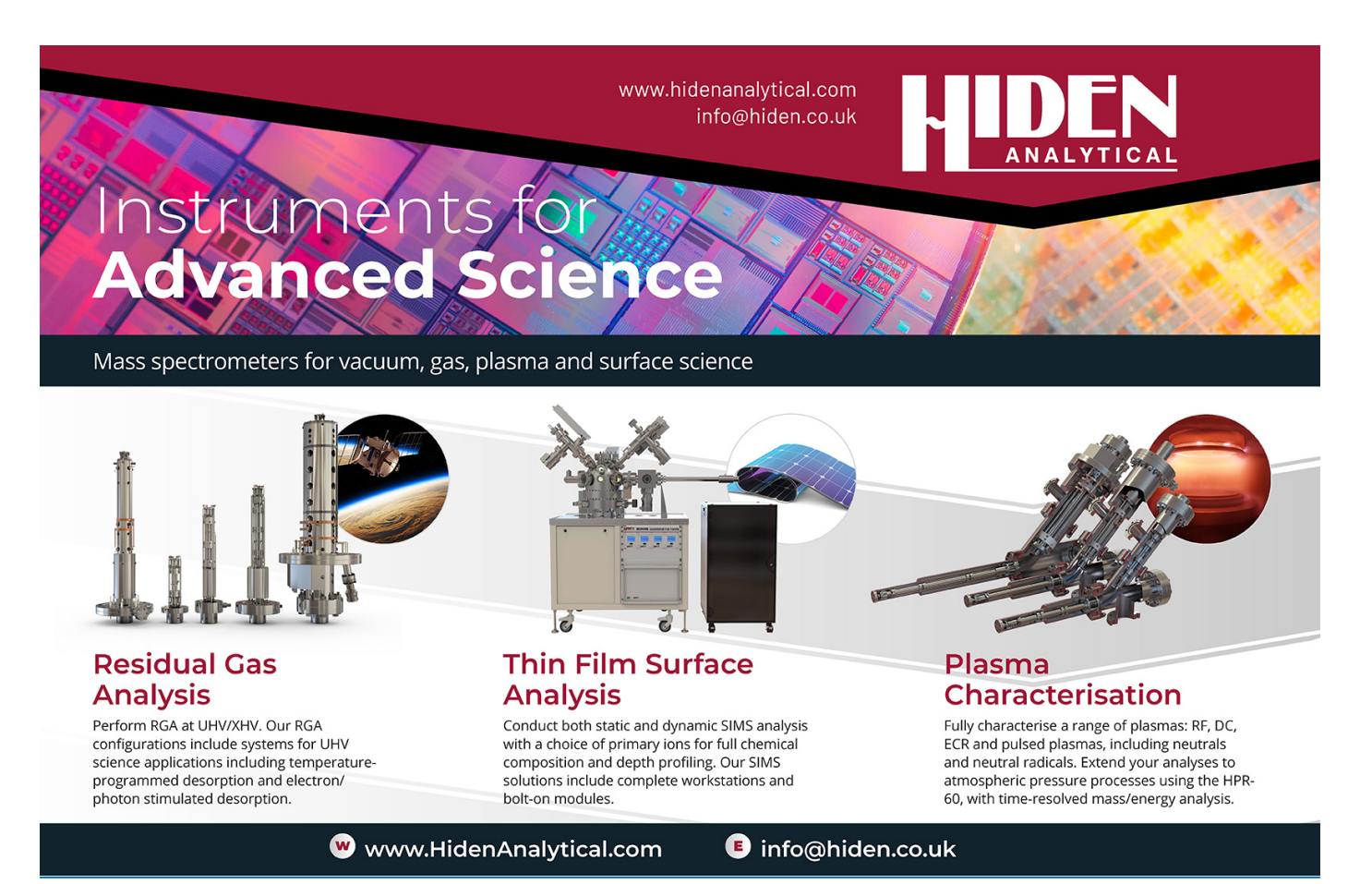
To cite this article: Richard Rotunno and Howard B Bluestein 2024 Rep. Prog. Phys. 87 114801

View the article online for updates and enhancements.

You may also like

- <u>Advances in applications of the physics of fluids to severe weather systems</u>

 Howard B Bluestein
- ARE GIANT TORNADOES THE LEGS OF SOLAR PROMINENCES? Sven Wedemeyer, Eamon Scullion, Luc Rouppe van der Voort et al.
- Examining the changes in the spatial manifestation and the rate of arrival of large tornado outbreaks
 Niloufar Nouri and Naresh Devineni



Rep. Prog. Phys. 87 (2024) 114801 (21pp)

https://doi.org/10.1088/1361-6633/ad7f6a

Report on Progress

Recent developments in tornado theory and observations

Richard Rotunno^{1,*} and Howard B Bluestein²

- ¹ NSF NCAR, Boulder, CO, United States of America
- ² University of Oklahoma, Norman, OK, United States of America

E-mail: rotunno@ucar.edu

Received 14 June 2024, revised 4 September 2024 Accepted for publication 25 September 2024 Published 8 October 2024

Corresponding editor: Dr Mark Geoghegan



Abstract

This article critically reviews research on tornado theory and observations over the last decade. From the theoretical standpoint, the major advances have come through improved numerical-simulation models of supercell convective storms, which contain the tornado's parent circulation. These simulations are carried out on a large domain (to capture the supercell's circulation system), but with high grid resolution and improved representations of sub-grid physics (to capture the tornado). These simulations offer new insights into how and why tornadoes form in some supercells, but not others. Observational advances have come through technological improvements of mobile Doppler radars capable of rapid scanning and dual-polarization measurements, which offer a much more accurate view of tornado formation, tornado structure, and the tornado's place within its parent supercell.

Keywords: tornado, supercell thunderstorm, fluid dynamics, mobile Doppler radar

1. Introduction

A tornado is a violently rotating column of air in contact with the ground. Tornadoes have been spawned in all types of convective storms (Bluestein 2013). The most violent tornadoes rotate cyclonically and occur within supercells (longlived, intense convective storms that have rotating updrafts). This article is focused on the tornadoes that form in supercells. As of the writing of The Fluid Dynamics of Tornadoes (Rotunno 2013), theoretical research on supercells and tornadoes had proceeded on two parallel paths. The present survey of developments in tornado theory over the past decade

Author to whom any correspondence should be addressed.

of the Creative Commons Attribution 4.0 licence. Any further distribution of this work must maintain attribution to the author(s) and the

title of the work, journal citation and DOI.

Original content from this work may be used under the terms

is largely about the convergence of these paths. Advances in tornado observations offered new ideas on how the tornado is formed within supercells and the variety of tornado flow fields. These advances have been largely a result of improvements in radar technology, particularly in the development of rapidscan, mobile, Doppler radars, especially those with polarimetric capability (Bluestein 2022).

On the one hand, modern supercell research dates from the 1940s when the routinely used surveillance meteorological radar detected the anomalous motion and shapes of certain radar echoes now known to be supercells (Marshall and Gordon 1957, Browning 1964). From that time through to the current day, correlations between routine observables in the pre-storm environment and supercell formation have informed both the theory and forecasting of these storms. In the 1970s, the advent of multi-Doppler radar observations and high-speed computer simulations of supercells, allowed objective verification of the simulated-supercell properties against observations (Klemp et al 1981). In the following decades, the simulations were analyzed, field experiments carried out and a relatively good understanding of the fluid dynamics of supercells was achieved (Klemp 1987), including the mechanisms for supercell updraft rotation about a vertical axis and its anomalous propagation; of relevance for tornadoes was the understanding of the main source of near-ground (sub-cloud layer) supercell rotation. For further information on supercells see Markowski and Richardson (2010) and Bluestein (2013).

On the other hand, the study of tornadoes, and more generally three-dimensional vortices, goes back much further than supercell studies in the history of fluid mechanics. To the casual (often terrified) observer, the tornado appears as a column of 'violently' rotating cloud, dust or debris. The columnar nature of most tornadoes motivates the view that the tornado has a high degree of axial symmetry (or 'axisymmetry'); some of the earliest and best-known solutions to the governing equations are for axisymmetric flow; the axisymmetric vortex forms the basis for the analytic study of vortex asymmetries (Dahl 2021). Laboratory studies of tornado-like vortices are based almost exclusively on an axisymmetric source of angular momentum imposed on an axisymmetric convergent flow.

As will be developed herein, the study of tornadoes within supercells faces several observational, theoretical, and computational challenges. One is the non-axisymmetric source of low-level supercell rotation; the source of low-level rotation in the supercell depends in some way on the side-by-side juxtaposition of streams of cool, dense air with warm, less-dense air interacting near the time of tornado formation (Markowski and Richardson 2010, chapter 8). The other difficulty has been the effect of surface friction which had been neglected in past supercell simulations because of the complications introduced, which are not necessary for the supercell, but potentially critically important for the tornado within it. Finally, past supercell simulations, although based on the principles of Large Eddy Simulation (LES), were executed with grid intervals too coarse to resolve motions within the inertial subrange of turbulence as required by LES (Wyngaard 2004).

Over the past decade or so, a new generation of highresolution supercell simulations including surface friction and, in some cases, resolved turbulence has started to examine the fluid dynamics of the largely axisymmetric, turbulent tornado in the context of its fundamentally non-axisymmetric sources of rotation in the parent supercell. This article critically reviews and evaluates the current ideas in this area, in addition to validating by observations certain aspects of tornado formation and structure made possible by the vastly increased temporal resolution of recently developed mobile radars and by other observing systems.

2. Idealized tornado-vortex models

To appreciate the developing confluence of ideas between tornado and supercell-with-tornado models, we first review the former to provide context for the latter. Idealized tornadovortex models are laboratory-inspired numerical simulations in which a tornado-like vortex (TLV) is generated by an axisymmetric converging flow imposed on an axisymmetric source of angular momentum characterized by the Swirl ratio S (the ratio of the imposed tangential to axial velocity, Rotunno 2013, R13, section 2.2). For constant viscosity, the Reynolds number Re and S are the two control parameters for these experiments. For fixed Re, the types of vortex motion vary as a function of S as illustrated in figure 1 which shows the flow in the axial-vertical plane for figures 1(a)–(c) (the tangential motion is generally maximized on the streamlines reaching nearest to the origin). For increasing S, the vortex structure changes from (a) single-cell to (b) single-cell below and two-cell (an updraft with a central downdraft) above to (c) two-cell; the latter may give rise to (d) multiple vortices.

Past axisymmetric numerical simulations of the vortices shown in figures 1(a)–(c) were done for $Re = O(10^3)$. Rotunno et al (2016) simulated cases with Re as high as 6.4×10^{5} for a range of S. They found laminar boundarylayer flow even for the highest Re implying that fully threedimensional simulations are required to allow for the onset and maintenance of turbulence. For the same physical setup as in the latter study, Nolan et al (2017) carried out LES (three-dimensional) experiments in which turbulence stresses are explicitly calculated. They found that that the boundary layer and other parts of the flow are turbulent and that the calculated stresses (momentum fluxes) act consistently with the downgradient-diffusion hypothesis implicit in axisymmetric, constant-viscosity simulations. For the most up-to-date studies along these lines see Wang et al (2023) which explores the effect of near-surface parameterized stress in these LES TLVs. The lower boundary condition on momentum is basically a drag law in the LES studies while the laminar experiments in Rotunno et al (2016) used the standard 'no-slip' (zero velocity) condition. Although the quantitative results for vortex structure are different, good qualitative agreement was found between the laminar-flow and LES/turbulence models.

To isolate the effects of a drag law in a simplified context, Fiedler (Fiedler 2017) revisited the axisymmetric numerical solutions of R13 with a constant viscosity, but using a drag law for the stress instead of a no-slip lower boundary condition. As the drag-law parameter could be varied from zero to infinity, solutions corresponding to the 'free-slip' (zero stress) to no-slip were found in addition to the range in-between ('semi-slip').

Figure 2 (after Fiedler 2017 Fluids) shows, for the same S and Re, the effect of the lower boundary condition on the velocity components (u^c, v^c, w^c) in the cylindrical coordinates (r, ϕ, z) and pressure variable p. In the free-slip case (top row), there is no boundary layer, the solution has a weakly rotating downdraft at the center (for all S) surrounded by strongly rotating upward motion (a 'two-celled' vortex as in figure 1(c)); the azimuthal velocity v^c is amplified by the conservation of angular momentum ($\Gamma = rv^c$) as fluid parcels are drawn radially inward by the applied buoyancy force (R13, section 3.2). As with the no-slip solution (section 3.3, R13), in the semislip case (bottom row; drag parameter set to produce solutions between the free- and no-slip limits), there is now a boundary layer in which intense radial inflow transports Γ closer to the center axis than in the free-slip case and, despite the diffusive loss of Γ to the surface, amplifies v^c to speeds

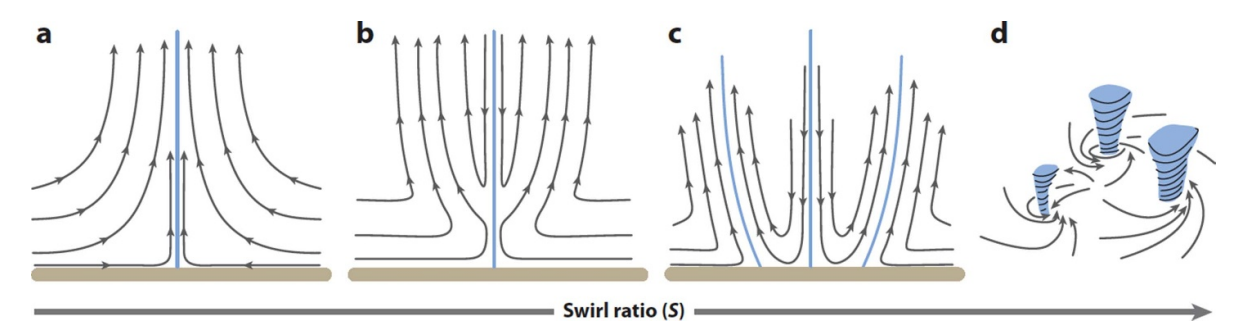


Figure 1. Vortex types as a function of Swirl Ratio S (R13; after Davies-Jones 1986). (Rotunno 2013). Reproduced with permission from the Annual Review of Fluid Mechanics, Volume 45 © 2013 by Annual Reviews, www.annualreviews.org.

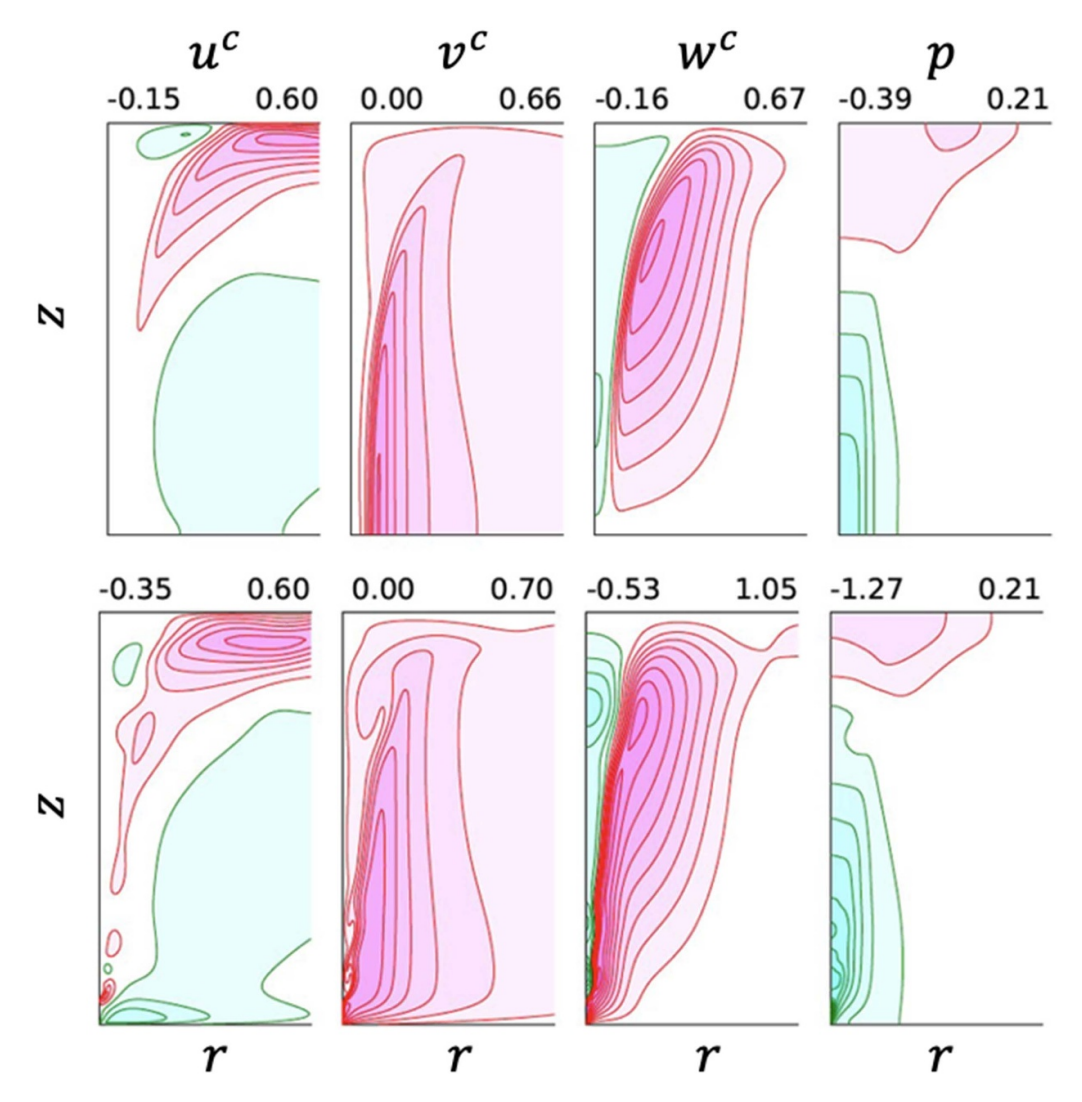


Figure 2. Steady-state axisymmetric simulations of tornado-like vortices free-slip (top row) and semi-slip (bottom row) lower boundary conditions. From left to right, the columns are the nondimensional radial, tangential and vertical velocities and pressure as functions of radius and height, with the minimum and maximum values at the top of each pane. Reproduced from (Fiedler 2017). CC BY 4.0.

which can be in excess of the free-slip case. Moreover, there is intense upward motion and low pressure associated with the convergent boundary-layer which results in an upward jet of intensely swirling flow (termed an 'endwall' vortex as in figure 1(b)) at the origin. Thus, the lower boundary condition can lead to qualitatively different types of TLV.

We emphasize here that the solutions for the two-cell vortex (figure 1(c)) are only slightly affected by the lower frictional condition and that therefore the free-slip two-cell solution (figure 1, top row) also represents a type of TLV (very wide, with a central downdraft). If the inner downdraft cell is sufficiently narrow, the TLV will appear as a one-celled

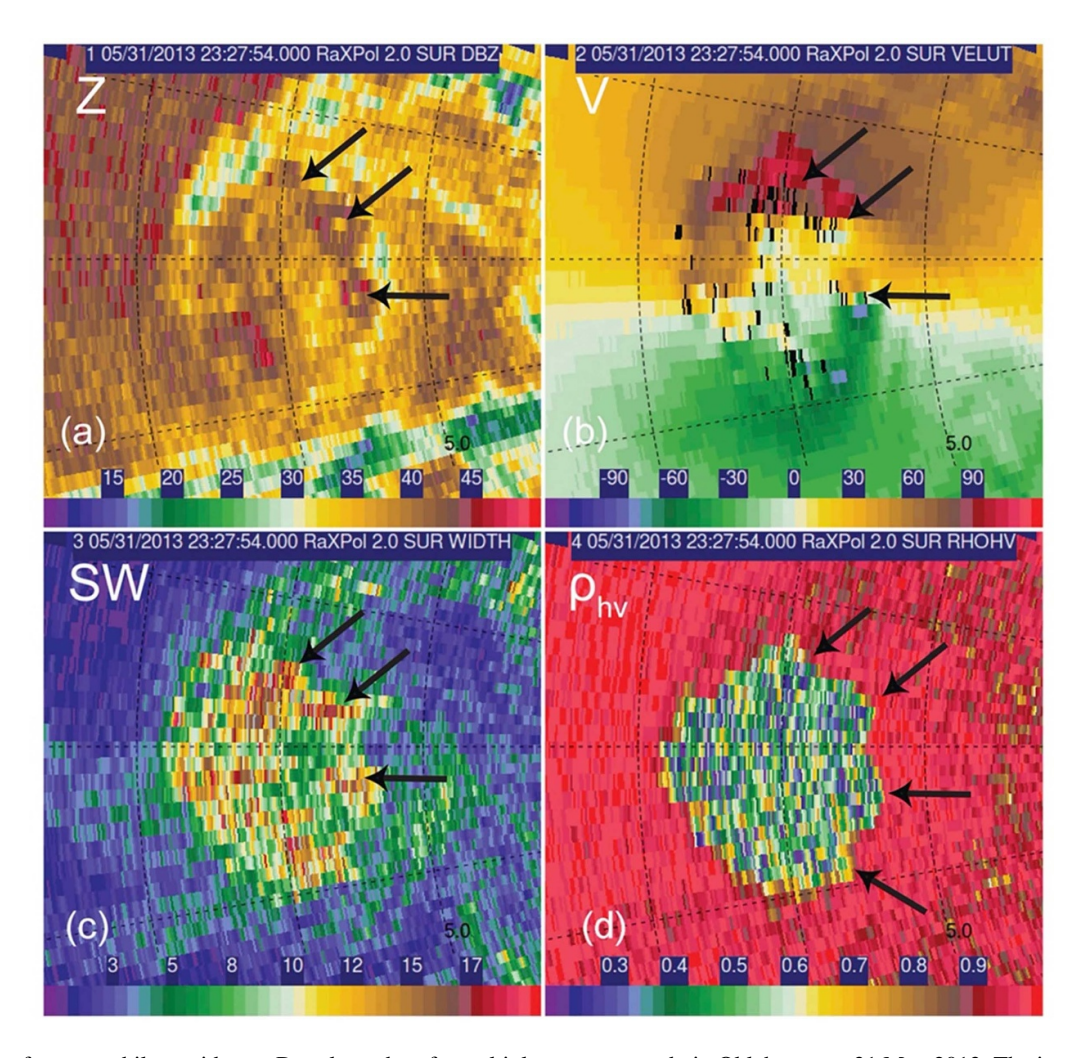


Figure 3. Data from a mobile, rapid-scan Doppler radar of a multiple-vortex tornado in Oklahoma on 31 May 2013. The intensity of the precipitation/radar signal intensity about the tornado is seen in (a), where the arrows point to three separate vortices within the larger tornado. Two of them exhibit weak-echo holes (WEH) created when debris and large precipitation particles are centrifuged radially outward. The color scale runs from relatively weak (green) to intense (red). Each vortex is seen also as a large radial shear in Doppler velocity in (b), where arrows point to the same three vortices noted in (a). Each vortex is also marked by relatively high spectral width (c), since the volumes sampled by the radar encompass higher ranges of Doppler velocities where there are vortices. In (d), a parameter that measures the (cross) correlation coefficient of the radar return in the horizontal and vertical plane shows that the overall tornado has a debris cloud (lower correlations due to tumbling), against a background of higher correlations (above 0.9). The arrows point to protuberances, each of which indicates a different debris cloud associated with each vortex. From Bluestein *et al* (2015). © American Meteorological Society. Used with permission.

vortex but with the vertical velocity maximum far above rather than near the surface. The importance of these distinctions will become clearer in the discussion of supercell simulations using free-slip and drag-law lower boundary conditions.

Three-dimensional instability of these axisymmetric vortices can sometimes lead to multiple vortices (figure 1(d)), each potentially having its own endwall structure with a strong pressure minimum above the ground. For this reason, these multiple vortices were originally termed 'suction' vortices, but later the 'suction' aspect was de-emphasized, and more recently, based on radar data, damage surveys, and modeling, emphasized again (Wakimoto *et al* 2022). Multiple vortices are prominent features in the observations described below (figures 3 and 4).

Because the radar data were collected every 2 s, and the vortices persisted for at most around 20–60 s, it was possible to track many of the vortices with respect to their parent, larger-scale circulation center, which was hitherto impossible with older radars, which scanned much more slowly (Bluestein et al 2018). Most of the long-lived vortices formed in the left-rear quadrant, near or just inside of the radius of maximum wind, in a region of high radial shear of the azimuthal wind of $\sim 0.01 \, \mathrm{s}^{-1}$ (figure 5). They then rotated around the center of the parent circulation center, and turned radially inward while they dissipated in the two forward quadrants. It was hypothesized that the radial-inward parts of the trajectories could have been due to the effects of surface friction (as in the second row of figure 2). Evidence was found that the multiple vortices either retrograded slowly with respect to the mean azimuthal flow

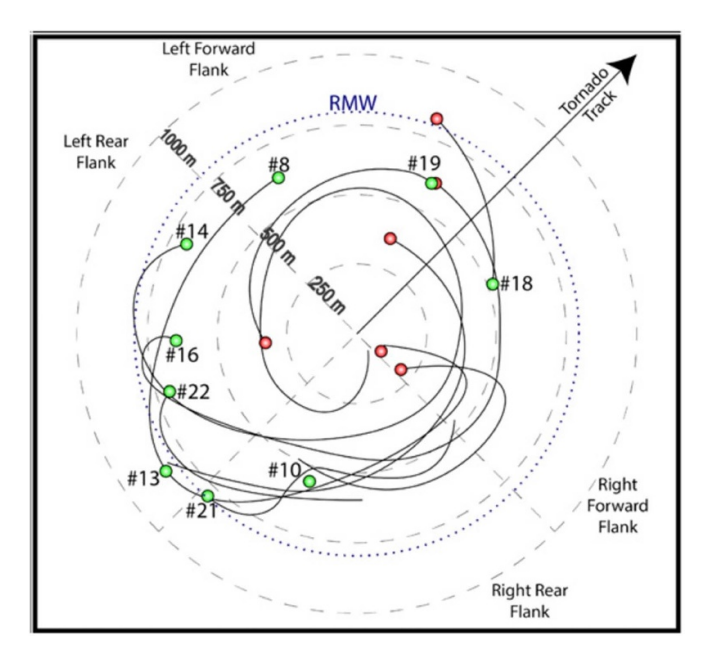


Figure 4. Smoothed tracks of 'secondary,' multiple vortices in a large tornado in Oklahoma on 31 May 2013. The green (red) circles mark the beginning (ending) of each vortex. From Bluestein *et al* (2018). © American Meteorological Society. Used with permission.

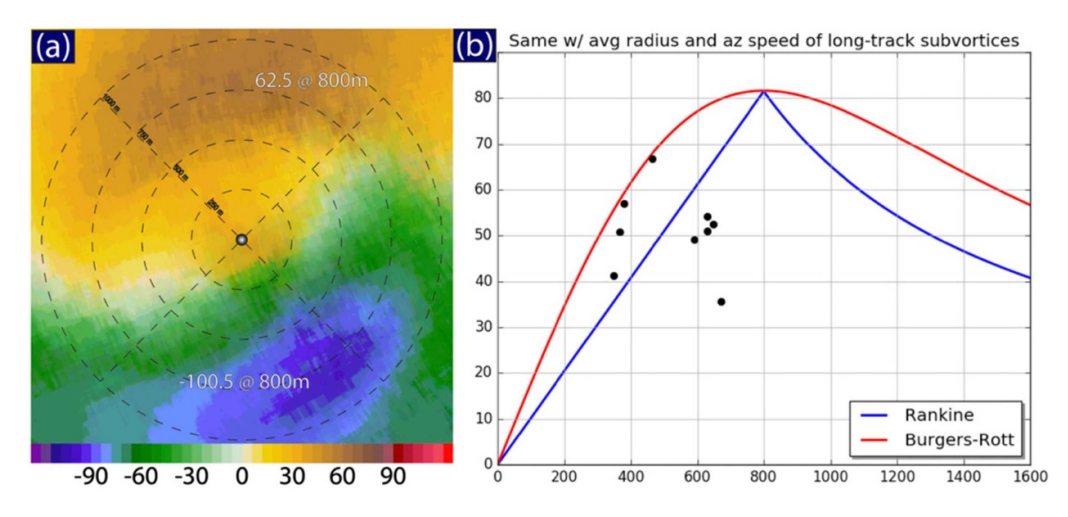


Figure 5. (a) Mean Doppler velocity as a function of distance from the center of the vortex in a tornado in Oklahoma on 31 May 2013 (see also figures 3 and 4). (b) Azimuthal velocity of long-lived vortices as a function of distance from the center (black dots) and Rankine and Burgers-Rott vortices fit to the Doppler data. From Bluestein *et al* (2018). © American Meteorological Society. Used with permission.

or moved along approximately with the mean azimuthal flow, which is consistent with the existence of vortex Rossby waves (Huang and Xue 2023), which are waves that can exhibit retrograde propagation on the radial gradient in vorticity of the axisymmetric azimuthal component of the wind (figure 5(b)). The ground-relative speed of some vortices was well in excess of $100~{\rm m~s^{-1}}$, in part due to the mean flow of the parent tornado and in part due to the mean tornado motion and is thought to be responsible for intense, but highly localized transient bursts of damage.

In the foregoing studies it is assumed that the tornado forms in a statically neutral environment with vertically constant ambient Γ . Parker (2012), using an axisymmetric setup (in a 3D model) similar the those described above, investigates the effect of static stability on tornado formation; an axisymmetric

heating is imposed to represent the convective storm with differing initial distributions of $\Gamma(r,z)$ to represent midlevel rotation. Among the interesting results is the effect of stability on the downward transport of Γ by compensating subsidence surrounding central updraft created by the imposed heating; this downward transport of Γ can stimulate a boundary-layer response shown as in the lower row of figure 2.

The latter result was anticipated in Davies-Jones (Davies-Jones 2008) in which a rainy downdraft at the periphery of the axisymmetric updraft transports Γ downward, which then initiates the boundary-layer processes leading to endwall-vortex TLV formation. We will describe this model in more detail below as it provides, we believe, the closest mathematical connections between the dynamics of supercells and tornadoes characterized by the endwall vortex (figure 1(b)).

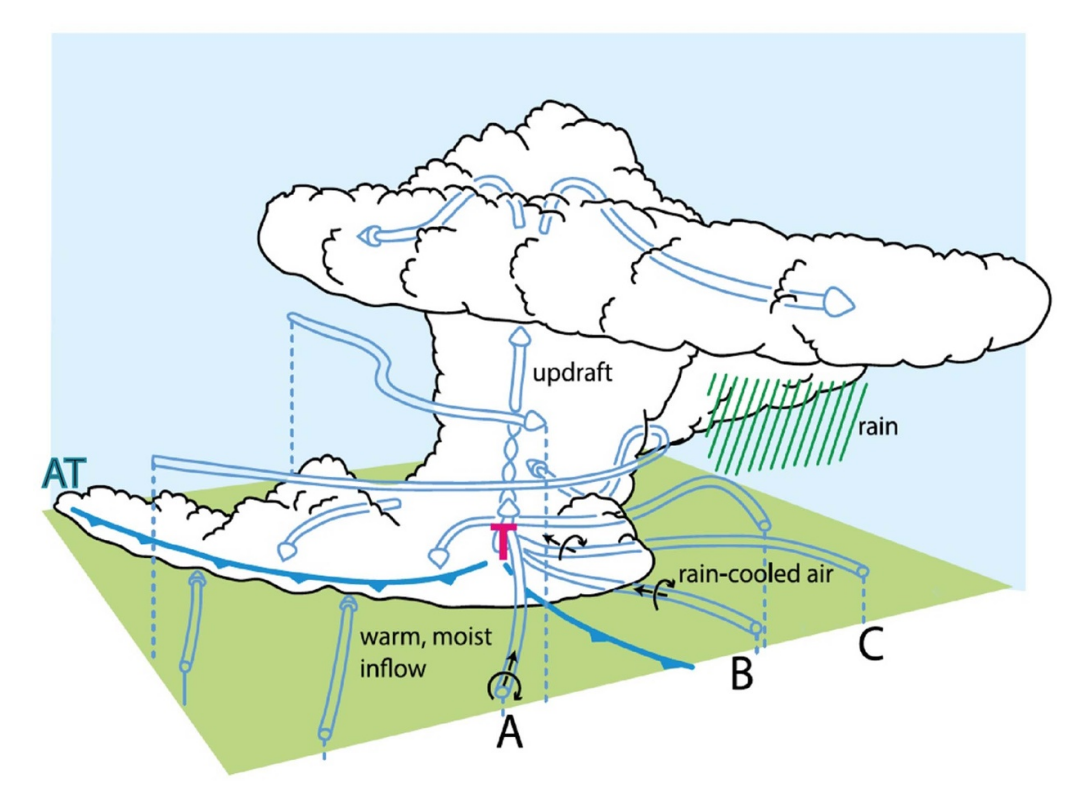


Figure 6. Schematic of the flow within and around a supercell (following Klemp 1987, Markowski and Richardson 2010, Rotunno *et al* 2017). Streamlines (A), (B) and (C) carry horizontal vorticity into the supercell updraft whereupon they tilt upward to form supercell rotation about a vertical axis. The typical location of the tornado is marked by the red 'T' and the (rarer) anticyclonic tornado by 'AT'. From Rotunno *et al* (2017). © American Meteorological Society. Used with permission.

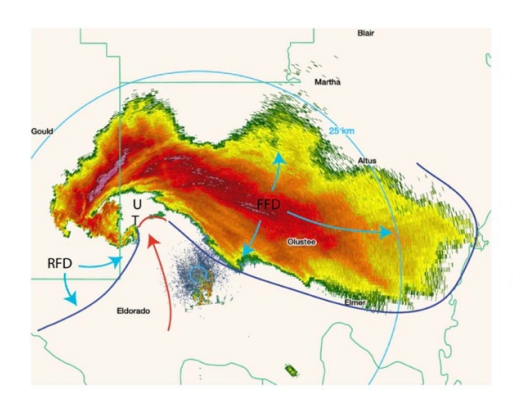
3. Supercells

Recent comprehensive reviews of supercell theory and observations can be found in Bluestein (Bluestein 2013, chapter 4) and Davies-Jones (Davies-Jones 2015). For the purposes of this review of tornado theory and observations over the last decade only a summary is given here of the characteristics of the mature supercell relevant to tornadoes following Rotunno (Rotunno 2013 section 1.2).

Figure 6 is a schematic diagram of the supercell. The supercell updraft is fed primarily by warm, moist environmental air (marked 'A'). The variation of the environmental wind with altitude (wind shear) implies a horizontal component of vorticity (or horizontal vorticity for brevity) in the direction along the inflowing air, which, when reoriented ('tilted') to the vertical by the updraft, produces rotation about a vertical axis at the low- to mid-levels of the supercell updraft (called a 'mesocyclone'). As a result of the wind shear, the precipitation falls to the downshear side of the updraft as illustrated; evaporation of this precipitation cools the air at low levels and thus creates a thermal boundary at and near ground level. This thermal boundary produces horizontal vorticity baroclinically on trajectories (B and C) directed toward the updraft along the thermal boundary; this baroclinically produced vorticity may be also tilted upward beneath the main storm updraft and produces updraft rotation about a vertical axis at near ground level (trajectory 'B'). Davies-Jones and Brooks (1993) found that the continued baroclinic production of horizontal vorticity can change the orientation of the vorticity with respect to the descending flow such that a parcel may arrive at the surface with enhanced vertical vorticity which can be amplified by vortex stretching below the updraft (trajectory 'C'). The typical location of the (cyclonic³) tornado is indicated by the red 'T'.

The foregoing description is largely based on the first generation of supercell simulations using simplified environmental wind profiles. The sources of rotation were and continue to be a central question in subsequent numerical studies of supercells. In recent years a more complete understanding of these sources based on a mathematically rigorous theory was developed in Dahl (2017) and Davies-Jones (2022). Among the results relevant to this review is the analysis of the effects of more complex and observationally pertinent environmental wind profiles have on low-level rotation (the flow represented by 'A' in figure 6) and the strength of the low-level updraft. These effects are discussed below.

³ Sometimes an anticyclonic tornado is found near the tail end of the flanking line marking the boundary between the outflow and the ambient warm, moist air (Bluestein *et al* 2016), which is indicated by the blue 'AT' in figure 5 (see also Markowski and Richardson 2014, their figure 25(a) reproduced in our figure 13). Recent Doppler-radar observations indicate that the anticyclonic tornado tends to form as the companion cyclonic tornado is dissipating, with some circumstantial evidence that a secondary downdraft surge coincident with it may be related to anticyclonic-tornado formation (Bluestein *et al* 2016, Margraf 2023).



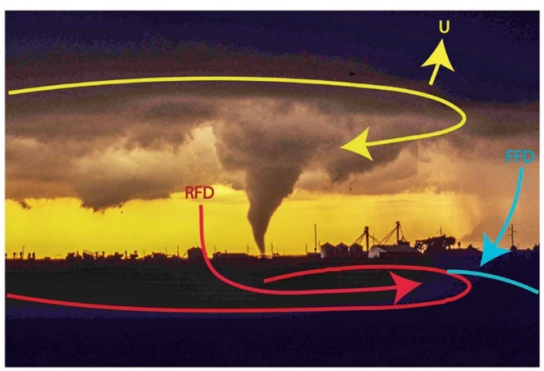


Figure 7. (a) Schematic diagram of the near-ground flow attending the typical intense tornado, superimposed upon the radar image (reflectivity; red/orange signifies the most intense precipitation and yellow/green denotes the least intense) of a tornadic supercell in southwest Oklahoma on 23 May 2024, courtesy of the second author). The tornado is located at T; the main updraft is centered near U (actually the updraft assumes a horseshoe shape about the sharply curved yellow streamline at the right); the rear-flank downdraft is centered near RFD; the forward-flank downdraft is located near FFD. (b) Tornado (cyclonic) in central Oklahoma on 24 April 2006, viewed to the west (photo courtesy of the second author). Other notation is as in (a).

Figure 7(a) shows a more detailed schematic picture of the near-ground flow in the immediately vicinity of an intense tornado. There are a forward- and rear-flank downdraft produced by the precipitation-cooled air. The warm, moist environmental air flows towards the supercell updraft where the warm air is occluded by the cold air. The tornado sits at the tip of the occlusion. Figure 7(b) shows a photograph of a tornado from a ground-level view (roughly from the 'A' location in figure 6), illustrating the tornado's position near or at the occlusion point. Cool air associated with precipitation can be seen in the background (right side of photo); warm, moist air flowing from behind the viewer is made visible as it rises to form the low cloud in the foreground. The cool and warm air streams appear to be wrapping around the tornado which itself is manifested by an axisymmetric cloud column on the curled-back cloud base in the background. The lower cloud base around the tornado is evidence of the powerful supercell updraft lifting cool, nearly saturated air to its lower condensation level.

Over the last decade, supercell research has been focused on how the physics of the apparently axisymmetric tornado is related to the parent supercell's low-level non-axisymmetric circulation. Early numerical simulations of supercell fluid dynamics produce the observationally recognizable features illustrated in figure 6 (Klemp 1987). These simulations were based on a free-slip lower boundary conditions which, as described with respect to figure 2 (upper row) or as in figure 1(c), can lead to a TLV without a boundary layer but with intense rotation at ground level about a nearly vertical axis (essentially a near-ground mesocyclone, see figure 13 of Klemp 1987). In contrast, idealized numerical simulations (figure 2, lower row, or figure 1(b)) and observations of certain tornadoes indicate that frictional ground contact ('semi-slip' lower boundary condition) is important, if not essential, to explain the observed features of these tornadoes more closely resembling the endwall vortex described above. Based on this understanding, the present review of tornadic supercell simulations is divided into a review of recent free-slip and semi-slip studies of supercell TLVs. Although available nowadays in textbooks (e.g. Markowski and Richardson 2010, Cotton *et al* 2011, Bluestein 2013), we next provide some context for numerical simulations and analysis of supercells with particular attention to the lower levels of the supercell where tornadoes are observed.

4. Numerical simulations of the tornadic supercell

4.1. Cloud model and analysis tools

The supercell is a type of convective storm (seen as a cumulonimbus cloud); these storms can be simulated through numerical solution of the equations of motion with representations of the phase changes of water substance (which affects the buoyancy through condensational heating and evaporative and melting cooling and water-substance loading) and turbulence (which affects scalar mixing and stress). All existing supercell simulations are three-dimensional. In the Cartesian coordinates (x,y,z) the dependent variables are the velocity field $\boldsymbol{u}=(u,v,w)$, temperature, pressure and water substance in its three phases. The equations of motion are,

$$\frac{\mathrm{d}\boldsymbol{u}}{\mathrm{d}t} = -\nabla p + B\boldsymbol{k} + \boldsymbol{F} \tag{1}$$

where p is the pressure variable, B, the buoyancy, F, the frictional force per unit mass and k the unit vector in the vertical direction. The buoyancy B is determined by numerical solution of the First Law of Thermodynamics considering the latent heating due to the phase changes of water substance and water-substance loading. Separate equations for the transport and conversion of the relevant categories of water (cloud, rain, ice) and the conservation of mass complete the equations of a cloud model (e.g. Bryan and Fritsch).

The equation for the vorticity $\omega = \nabla \times \mathbf{u} = (\xi, \eta, \zeta)$ is found by taking the curl of (1),

$$\frac{\mathrm{d}\omega}{\mathrm{d}t} = (\omega \cdot \nabla) u - k \times \nabla B + \nabla \times F \tag{2}$$

where for the purposes of this review we have assumed that the flow may be approximated as incompressible $(\nabla \cdot \boldsymbol{u} = 0)$. The basic tool for understanding the rotational characteristics of the supercell is to solve (2) for ω given \boldsymbol{u} , \boldsymbol{B} and \boldsymbol{F} from either the cloud-model solution or a hypothetically simpler flow that captures some of the basic features of the supercell. Note that although supercells are frequently referred to as supercell thunderstorms, storm electricity is not considered significant, and its effects are therefore absent from these equations.

The basic puzzle is that a supercell can form in environments rich in horizontal vorticity but with zero vertical vorticity $[\omega = (\omega_h, 0)]$ thus motivating a theory for how a supercell updraft can develop rotation about a vertical axis, a hallmark of the supercell. The other unique feature of the supercell is its ability to live longer than it takes an air parcel to ascend to the top of the storm and either exit through the anvil or fall to the ground with precipitation, and also to propagate with respect to the environmental winds in the cloud-bearing layer; the analysis of this feature requires an examination of the solution of (1), particularly the behavior of the pressure p attending a rotating updraft (Rotunno and Klemp 1985). Using (2) and a cloud-model solution, figure 6 shows how the first term on the right-hand side of (2) can redirect ω_h (at low levels) to the vertical through the tilting action of the supercell updraft w_{up} $[(\omega_h \cdot \nabla_h) w_{up}]$; the supercell propagation [analyzed through (1)] is taken into account by the storm-relative perspective of figure 6. The combination of propagation and ambient horizontal vorticity gave rise to the concept of streamwise vorticity (Davies-Jones 1984) which has been shown to be a very effective supercell-forecast parameter (next section). The second term of the rhs of (2) shows that the buoyancy distribution produced by evaporative cooling of rain can produce an entirely different direction to the local ω_h which can be subsequently redirected upward through the first term on the right-hand side of (1).

Another analysis tool is Bjerknes' Circulation Theorem which follows from the integral of (1) on a closed material curve, viz.,

$$\frac{\mathrm{d}C}{\mathrm{d}t} = \oint (B\mathbf{k} + \mathbf{F}) \cdot \mathrm{d}\mathbf{s} \tag{3}$$

where the circulation $C = \oint \mathbf{u} \cdot d\mathbf{s}$ and $d\mathbf{s}$ is a line element tangent to the curve. Equation (3) was originally used in Rotunno and Klemp (Rotunno and Klemp 1985) to show that the baroclinic effect of the cold pool was the fundamental cause of near-ground circulation in a supercell. Where data are available this result has been confirmed by observations (Markowski *et al* 2012, their figure 1). Although we will refer to circulation along the way, this review will focus less on circulation than vorticity because the circuits become extremely convoluted when followed far enough backward in time with

high spatial resolution in the presence of small-scale flow perturbations. Moreover, circuits will almost invariably dip below the lowest grid level of the model and infect the calculations with numerical error (see Davies-Jones and Markowski 2021 MWR where a method is developed to compute the circulation on a non-material line that is constrained to remain above the lowest grid level). The effects of surface friction (3) on circulation warrant special consideration to be given below

The mathematical analysis of (2) and (3) has reached an advanced state through the work of Davies-Jones (Davies-Jones 2022 and refs.) based on Lagrangian parcel dynamics. While the formulas are too complex for this review, some of the basics results will be referred to in the interpretations of recent simulation studies.

4.2. Tornadic supercell environments

Although most tornadoes occur within supercell storms, not all supercells produce tornadoes. The consensus in the literature is that, given sufficiently large convective available potential energy (CAPE) and low convective inhibition (CIN), the environmental wind profile is the most important discriminator for the tornadic supercell. The environmental wind profile is most often displayed in the form of a hodograph (Markowski and Richardson 2010, chapter 2.7, Bluestein 2013, Chapter 4.5) displaying the south-to-north wind V(z)versus the west-to-east wind component U(z) with altitude z as a parameter (figure 8). On a hodograph V = V(U), so the direction of the shear vector is the tangent to the hodograph line since $\left(\frac{dU}{dz}, \frac{dV}{dz}\right) = \frac{dU}{dz} \left(\boldsymbol{i} + \frac{dV}{dU}\boldsymbol{j}\right)$; the environmental vorticity $\left(-\frac{dV}{dz}, \frac{dU}{dz}\right) = \frac{dU}{dz} \left(-\frac{dV}{dU}\boldsymbol{i} + \boldsymbol{j}\right)$ which is 90° to the left of the shear vector. Figure 8 shows a typical supercell hodograph; a distinguishing feature of the supercell is that its motion (marked by the storm-motion vector \mathbf{c}) is off the hodograph line and across the wind shear which means that there is supercell-relative flow as indicated by the black arrows. With a reasonable guess or observation (typically based on radar-echo movement) of c one can estimate the magnitude of the rotation on the streamline flowing into supercell as depicted for streamline 'A' in figure 6. An empirical measure of the net effect of this streamwise vorticity entering the supercell is given by,

$$SRH(\mathbf{c}) = \int_{0}^{h} (\mathbf{v} - \mathbf{c}) \cdot (\nabla \times \mathbf{v}) \,dz, \tag{4}$$

Storm-relative helicity (SRH) where the environmental $\mathbf{v}(z) = [U(z), V(z), 0]$, \mathbf{c} is the storm-motion vector and h is an empirically determined top on the inflow layer (typically 3 km) (Bluestein 2013). In terms of figure 8, $(\mathbf{v} - \mathbf{c}) \cdot (\nabla \times \mathbf{v})$ is optimally configured when the black and blue arrows align. For a full theoretical account of the foregoing and other factors affecting vorticity in a supercell see Davies-Jones (Dahl 2017).

There is a growing observational consensus that larger values of SRH can discriminate between tornadic and nontornadic supercells through larger |v-c| and/or a more favorable alignment of relative velocity and ambient vorticity over the layer depth. Estimates of the SRH over the lowest few

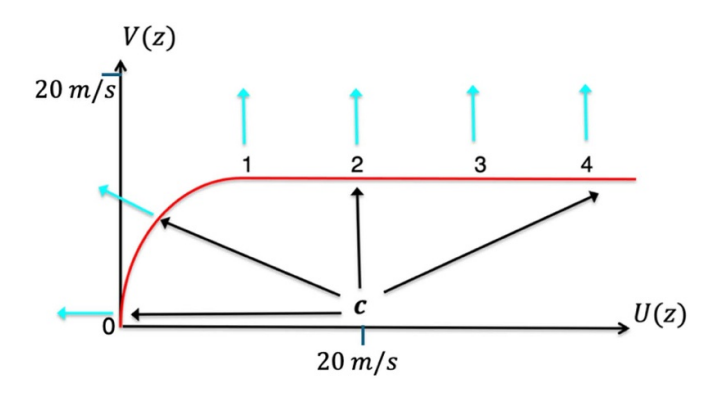


Figure 8. Hodograph for a tornadic supercell (red line), storm-relative motion vectors (black) and environmental vorticity vectors (cyan) at z = 1, 2, 3, 4 km AGL. Typical wind values are indicated on the axes.

hundred meters and over the lowest 6 km, combined with thermodynamic indices CAPE and lifted condensation level make up the Significant Tornado Parameter or STP (Thompson et al 2004 Wea. Forecasting; Esterheld and Giuliano 2008 Electronic Journal of Sever Storm Meteorology; Grams et al 2012 Wea. and Forecasting, Nowotarski and Jensen 2013 Wea. Forecasting; Parker 2014 Mon Wea Rev, Sherburn and Parker 2014 Wea. Forecasting; Wade et al 2018 Mon Wea Rev, Nowotarski and Jones 2018 Wea. and Forecasting, Coffer et al 2019 Wea. and Forecasting; Coniglio and Parker 2020 Mon Wea Rev, Bunkers et al 2022 Wea. and Forecasting).

Numerical simulations have largely succeeded in capturing this observed environmental sensitivity (section 4.5). Evidence from these simulations indicate that SRH concentrated over the lowest few hundred meters produce strong low-level rotation; the attending low pressure enhances the supercell updraft at low levels providing greater horizontal convergence (Coffer *et al* 2023, *Mon Wea Rev*). This research shows that the low-level inflow environment vorticity, characterized by the SRH, (trajectory 'A' in figure 6) plays a crucial role in tornadogenesis.

The recent simulations of tornadic supercells described below all use some variation on the tornado-favorable environmental wind profile shown in figure 8 as well as the other factors that comprise the STP.

4.3. Free-slip supercell simulations

Wind profiles such as those in figure 8 present a challenge for supercell simulations having frictional contact with the ground. The simplest problem to consider is an initial condition with a horizontally homogeneous wind profile [U(z),V(z),0], which satisfies the steady-state equations (1). However, surface stress can produce an evolution of the initial profiles even in the absence of a storm that can severely complicate interpretation. At the ground surface, the tangential stress (τ_{xz}, τ_{yz}) is typically given by the drag law,

$$(\tau_{xz}, \tau_{yz}) = \rho C_D \sqrt{u^2 + v^2} (u, v) @ z = \delta,$$
 (5)

where $z = \delta$ is the height of the surface layer (typically anemometer level), $C_D = \left(\kappa/\ln\left(\frac{\delta}{z_0}\right)\right)^2$ is the drag coefficient, z_0 is the roughness length, κ is von Kármán's constant and ρ is the air density. Assuming the standard stress–strain relation, the interior stress is given (for w = 0) by,

$$(\tau_{xz}, \tau_{yz}) = \rho \nu \left(\frac{\partial u}{\partial z}, \frac{\partial v}{\partial z}\right),$$
 (6)

where ν is the (eddy) kinematic viscosity and ρ the density. For the standard free-slip (zero stress) condition, (6) requires $\left(\frac{\partial u}{\partial z}, \frac{\partial v}{\partial z}\right) = 0$ which is not generally the case for the environmental $\left(\frac{\partial U}{\partial z}, \frac{\partial V}{\partial z}\right)$. Thus, if $\left(\frac{\partial U}{\partial z}, \frac{\partial V}{\partial z}\right) \neq 0$ at z = 0, then the stress derivatives $\frac{\partial}{\partial z} \left(\tau_{xz}, \tau_{yz}\right) \neq 0$ at z = 0, which will accelerate the wind even without any of the other forces active in (1). For this reason, the free-slip condition used in supercell-simulation models is

$$\frac{\partial}{\partial z}(\tau_{xz}, \tau_{yz}) = 0 \text{ at } z = 0.$$
 (7)

In a finite-difference grid-point numerical model, either the traditional free-slip condition $(\tau_{xz}, \tau_{yz}) = 0$ or that given by (7) act to extrapolate the vertical vorticity $(\varsigma = \frac{\partial v}{\partial x} - \frac{\partial u}{\partial y})$ of the interior to z = 0. In these free-slip simulations the frictional force F is just that due to parametrized turbulence or any implicit diffusion which does not generally play a major role in interpretation. In contrast, the semi-slip condition makes F a major contributor in the dynamics of the flow near the ground; these simulations are discussed separately in the next subsection.

The main application of the free-slip supercell simulations is to understand how the first two terms on the rhs of (2) act to produce vertical vorticity. Figure 9 (Dahl et al 2014) is a schematic diagram based on an analysis of (2) for a simulated supercell. The vorticity ω is decomposed into a 'barotropic' (environmental) and a 'baroclinic' (generated by internal buoyancy gradients) component. The black line represents the trajectory of a fluid parcel that reaches the vertical vorticity maximum (the TLV). The environmental hodograph used is like that of figure 8 so that the barotropic environmental vorticity (red arrow) aligns with inflow velocity. On approach to the cold air, the trajectory, in response to the high pressure of the cold pool and low pressure of the updraft, curves to the left and thus rotates the environmental vorticity with it (the 'river-bend' effect, i.e. the redirection of the horizontal vorticity by deformation with no change to the vertical vorticity, see e.g. Davies-Jones 2017). Upon entry into the cold air the baroclinic vorticity points to the left of the trajectory; however, as the trajectory begins to flow parallel to the cold air, baroclinic production of vorticity and further alignment by the local flow produces streamwise vorticity composed of both the original barotropic environmental vorticity and the baroclinic enhancement.

Figure 10 from Dahl *et al* (2014) shows that the vorticity acquires a positive vertical component ($\zeta > 0$) as the trajectory descends through the cold pool and levels off on approach to

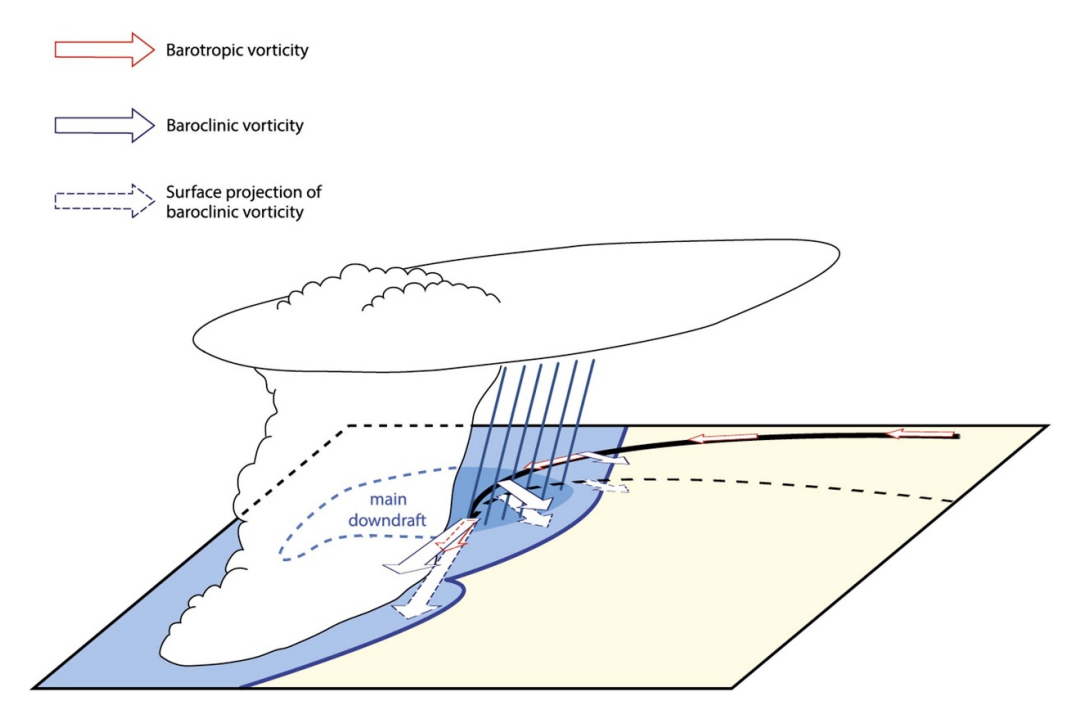


Figure 9. Schematic diagram of a simulated supercell with free-slip conditions (Dahl *et al* 2014). The black curve is the trajectory of an air parcel reaching the location of maximum vertical vorticity (the dashed line is its surface projection); the red arrows indicate the 'barotropic' (environmental) vorticity flowing into the storm which may be horizontally reoriented by the baroclinic effects of the cold pool; the blue arrows represent the vorticity produced baroclinically along the cold-air boundary. From (Dahl *et al* 2014). © American Meteorological Society. Used with permission.

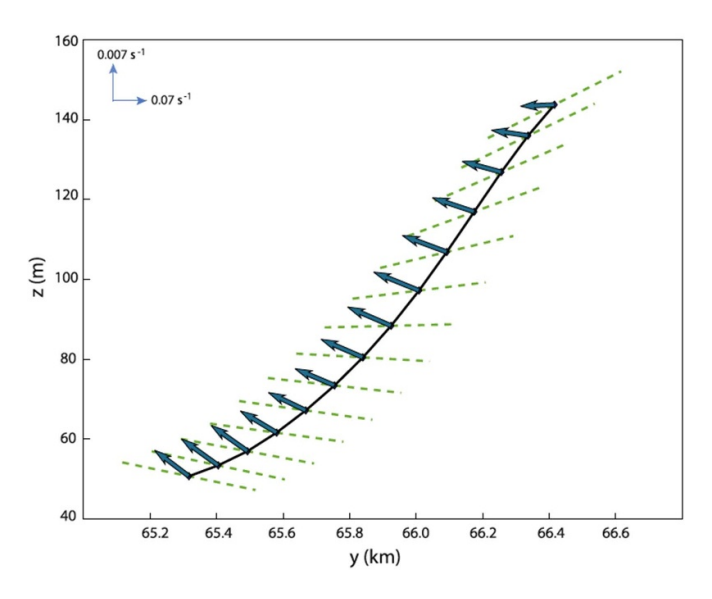


Figure 10. A portion of the trajectory shown in figure 9, which is descending, and on which the baroclinically produced vorticity (arrows) develops a component perpendicular to Lagrangian line elements (dashed). From (Dahl *et al* 2014). © American Meteorological Society. Used with permission.

the ground (as on trajectory 'C' in figure 6), which is referred to as a 'river' as it appears to feed the developing TLV (see also Dahl 2015).

Trajectories neighboring the ζ river, which have velocity and vorticity in alignment, are called the streamwise vorticity currents or SVCs (for further explanation, see Schueth

et al 2021); we interpret this feature as analogous to trajectory 'B' in figure 6. Figure 11 from Orf et al (2017) shows the volume-rendered vorticity magnitude from the perspective of an observer at position 'A' in figure 6; note how the SVC becomes a series of vortices (a ζ river) standing upright at the lower boundary which may be a manifestation of upward tilting in a descending current illustrated in figure 10 as they circle around the updraft center. It is not clear why there should be discrete vortices in the river, but we suspect that there is a line of shear vorticity that breaks up into individual vortices owing to shear instability. It should be noted that the relation of the SVC to the TLV or to the ζ river is under active investigation.

Further simplification of the problem is achieved by modelling the supercell updraft as a prescribed heat source and its rainy outflow as a heat sink shown in figure 12 (Markowski and Richardson 2014). The effects of supercell propagation are accounted for by fixing the location of the heat source and sink so that all the environmental motion is relative to it (like moving the hodograph curve in figure 7 to the left such that c = 0.)

This model produces results that are qualitatively and quantitatively similar to those from a cloud model. For example, analysis of the vorticity along the trajectory (red line) in figure 13 gives results similar to those from the cloud-model (Dahl *et al* 2014) described in figure 9.

One of the advantages of this model is that one has greater control over the input parameters.

For example, Parker and Dahl (2015) examined the effect of just the heat sink for various environmental winds finding, as in more-complicated flows, that a parcel descending through

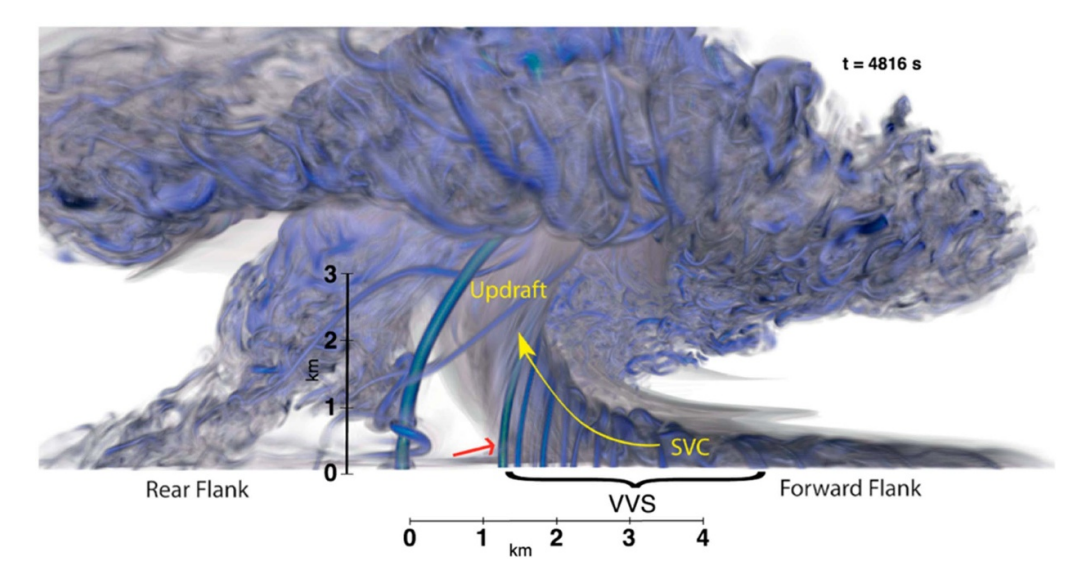


Figure 11. A volume-rendering of vorticity magnitude before the tornadogenesis. The yellow arrow gives the general motion of the features making up the Streamwise Vorticity Current (SVC); the red arrow points to the vortex that subsequently becomes the tornado. From Orf *et al* (2017). © American Meteorological Society. Used with permission.

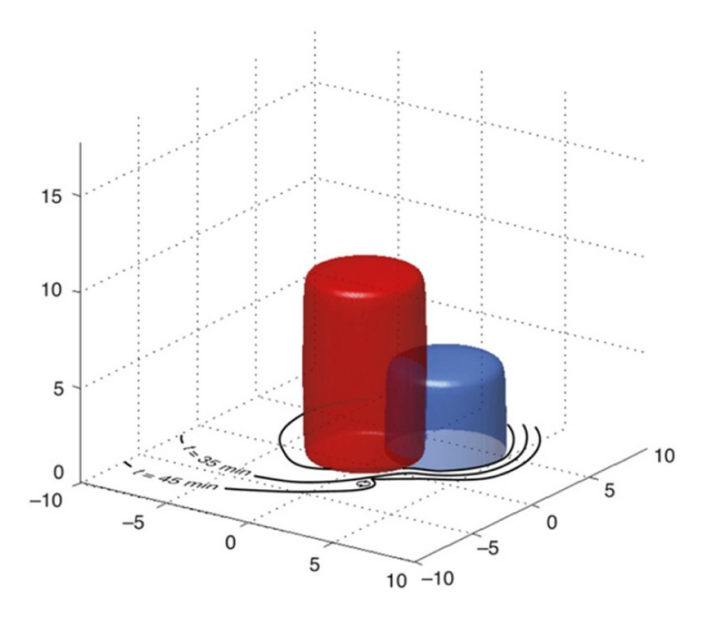


Figure 12. Idealized heat source and sink meant to emulate supercell processes. From Markowski and Richardson (2014). © American Meteorological Society. Used with permission.

the cold air acquires positive vertical component ($\zeta > 0$) as in figure 10 and, moreover, the environmental wind shear is not essential, just the heat-sink-relative flow.

Using the same model as MR14, Rotunno *et al* (Rotunno *et al* 2017) revisited the idea that ζ must be positive at the nadir of the trajectory feeding the TLV (red line in figure 9) and find that ζ can be zero at the nadir since large stretching along the SVC amplifies the horizontal vorticity to be tilted into the storm updraft (as for trajectory 'B' in figure 6). Boyer and Dahl (2021) found this mechanism in all their simulations but hypothesized that it would only occur after the formation of a

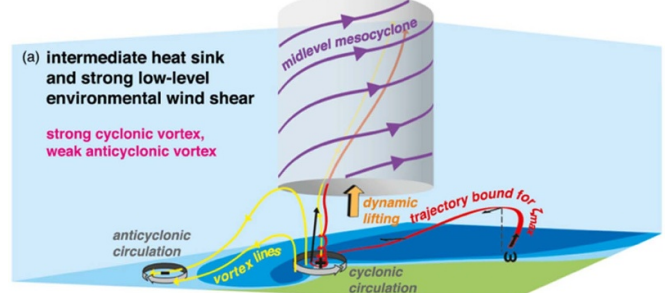


Figure 13. Idealized supercell-model solution showing rotating updraft, cold pool, a TLV, and an anticyclonic circulation (site of a potential anticyclonic TLV). From (Markowski and Richardson 2014). © American Meteorological Society. Used with permission.

TLV. The result found in Rotunno *et al* (2017) was anticipated by Naylor and Gilmore (2014) in a sensitivity study using a cloud model comparing tornadic and non-tornadic supercells.

At this point it worth re-emphasizing that the free-slip supercell simulations described in this section can produce TLVs only of the two-celled variety⁴ (figure 1(c)) and, in certain high-resolution studies, multiple vortices (figure 1(d)).

4.4. Semi-slip supercell simulations

The horizontal component of (1) can be written as

$$\frac{\mathrm{d}\boldsymbol{u}_{\mathrm{h}}}{\mathrm{d}t} = -\nabla_{\mathrm{h}}\varphi + \frac{1}{\rho}\frac{\partial\boldsymbol{\tau}_{\mathrm{h}}}{\partial z} + \boldsymbol{K} \tag{8}$$

⁴ If the core of the two-celled vortex is narrow enough in a model with horizontal diffusion, the two-celled vortex will appear as a one-celled vortex but without the signature boundary-layer circulation.

where $\tau_h = (\tau_{xz}, \tau_{yz})$ and only the vertical derivative of the horizontal stress is shown since it represents the effect of surface drag. For a horizontally invariant initial flow, the first terms on the right and left sides of (8) are zero; however, as discussed in section section 4.3, a semi-slip (surface drag) condition generally makes the stress-derivative term nonzero. In idealized modeling studies the 'fictitious' force K is added to cancel the stress-derivative term associated with the environmental flow [U(z),V(z),0]. Davies-Jones (Davies-Jones 2021) pointed out several unintended consequences (such as producing a spurious source of vorticity) of this modeling device that we will keep in mind as we review the current generation of supercell simulations using a semi-slip lower boundary condition.

One way to avoid the artificial force of (8) is to use a numerical weather-prediction (NWP) model with resolution high enough to simulate a tornadic supercell. An NWP model includes all the relevant physical processes but at the cost of added complexity such as a non-stationary environment; although the larger-scale motions are evolving, presumably they do so slowly compared to the time for tornadogenesis. Using multiply nested grids in an NWP model with horizontal grid distances as small as 50 m, Schenkman et al (Schenkman et al 2014) simulated the 8 May 2003 Oklahoma City tornadic supercell; figure 14 is their conceptual model based on analysis of the model output. As in the free-slip simulation (figure 9) there is warm inflow with streamwise vorticity encountering cool air with flow that turns cyclonically from the forward flank to the rear-flank (figure 14(I)). In the second and final stages (figures 13(II)–14(III)), the cold-air wraps cyclonically around the developing TLV. Friction with the ground creates horizontal vorticity pointing to the left of each airstream; these vortex lines converge towards the circulation center and are redirected upward forming the TLV. Tao and Tamura (Tao and Tamura 2020) using a different mesoscale model for another case came to substantially similar conclusions. Other notable studies using an NWP model include Mashiko (Mashiko 2016) and Mashiko and Niino (Mashiko and Niino 2017). Using nested grids with a 10 m grid interval in the innermost grid, the latter study simulates multiple vortices (which were observed in the case studies).

Roberts *et al* (2016, 2020) investigated the effect of drag in an idealized supercell using the modeling device in (8). Figure 15 shows the conceptual model for tornadogenesis that emerges from their simulation and analysis. In the three scenarios of figure 15, the cold pool is notably absent, and the updraft is not specifically shown, although its presence can be inferred by the upward tilting of the vortex lines. The vorticity budgets following a trajectory in these scenarios show the dominant contribution from surface friction in the production of horizontal vorticity that then is tilted upward in the developing TLV. Later idealized supercell simulations and analysis by Dahl and Fischer (Dahl and Fischer 2023) (judging the effects of the artificial force to be small) support the importance of frictional vorticity generation with respect to the TLV.

Based on rapid-scan mobile Doppler radar data from a major tornado in Oklahoma (Houser *et al* 2016; their figure 19)

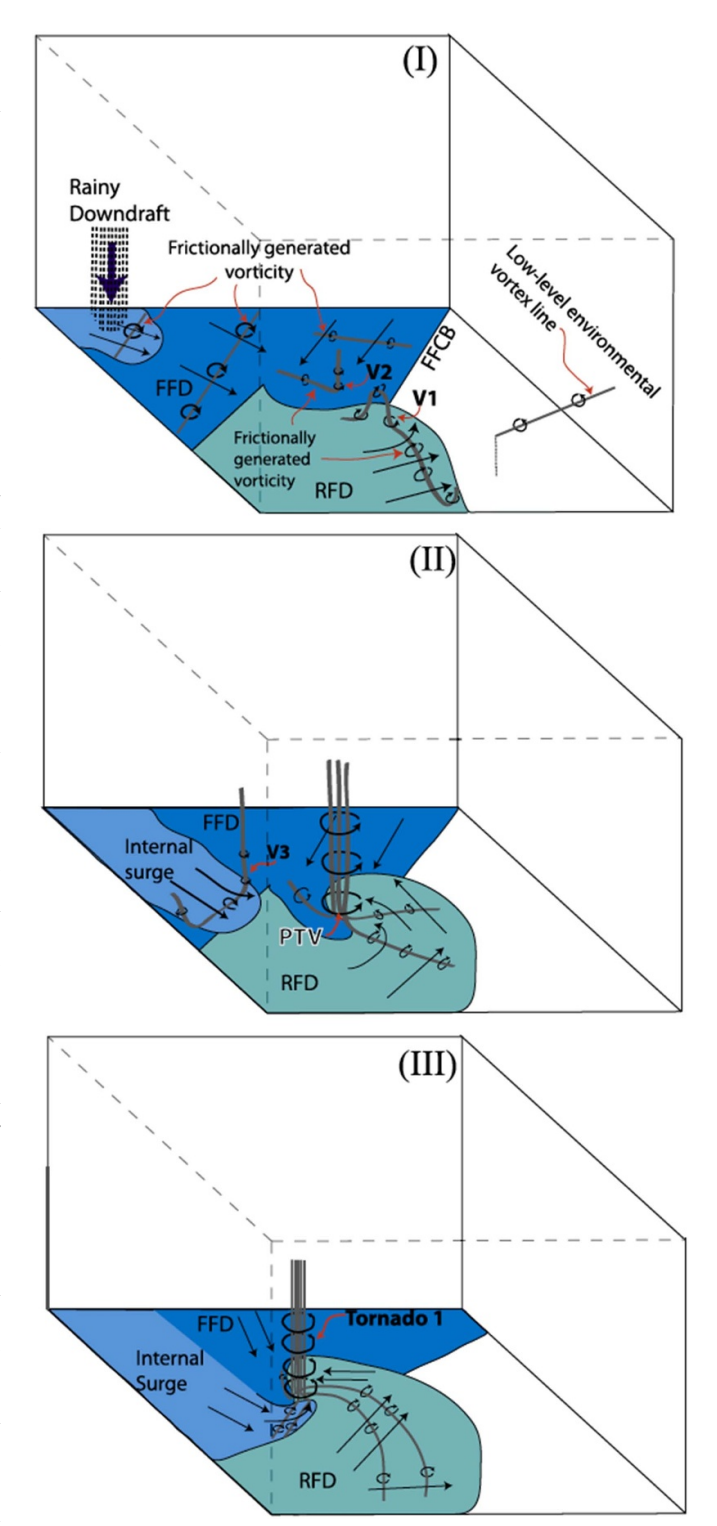


Figure 14. Conceptual model of tornadogenesis based on a numerical weather prediction model forecast of the 8 May 2003 Oklahoma City tornadic supercell. From Schenkman *et al* (2014). © American Meteorological Society. Used with permission.

it was speculated that the frictional generation of horizontal vorticity along the rear-flank gust front (RFGF) produced a weak-reflectivity band parallel to the RFGF and was correlated with the intensification of the tornado and a visible horizontal roll.

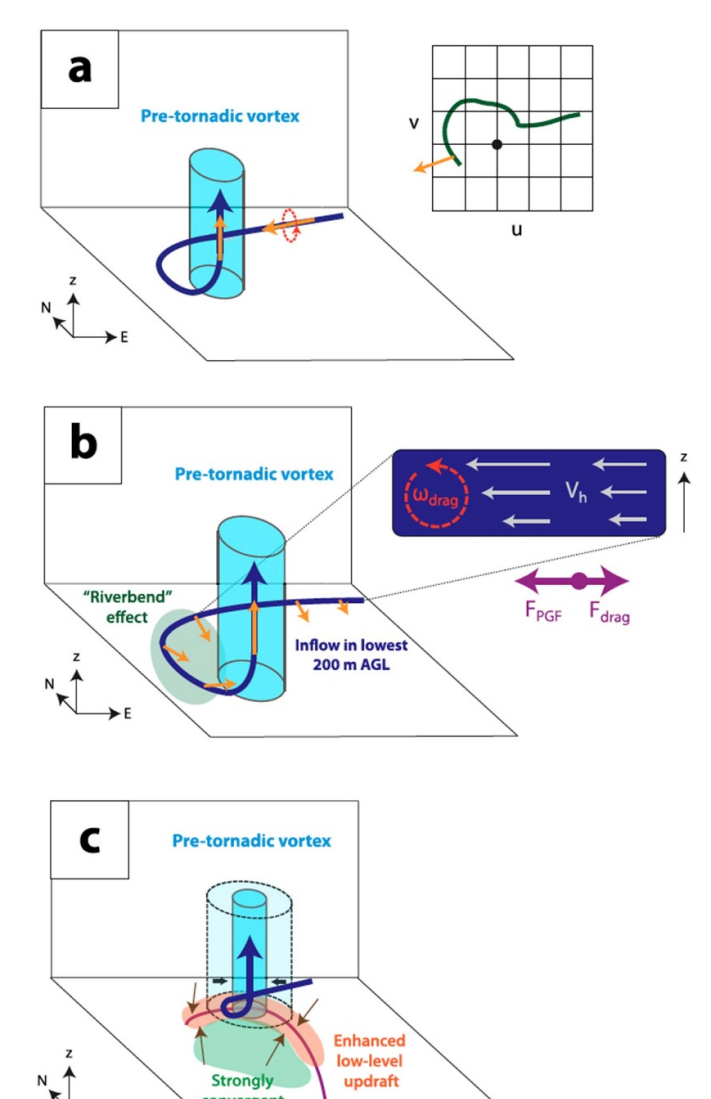


Figure 15. Conceptual model of tornadogenesis based on high-resolution supercell simulations. The yellow arrows represent the 3D vorticity vectors. From Roberts *et al* (2016). © American Meteorological Society. Used with permission.

flow

An analysis of the relative roles of vorticity production through baroclinic and surface-drag effects was done in Fischer and Dahl (Fischer and Dahl 2022). Their findings are summarized in figure 16. This diagram shows a two-step process wherein the horizontal vorticity (small blue arrows) on the air parcels that will form the TLV evolves according to the processes identified in free-slip simulations in figure 9 (figure 16(a)). As the low-level circulation develops, its interaction with the semi-slip lower boundary (figure 16(b)) produces a convergent flow that concentrates the vortex lines and streamlines to a common center producing the TLV. Further refinement of these ideas can be found in Fischer *et al* (2024)⁵.

Markowski (Markowski 2024) using an idealized cloud model with resolved boundary-layer turbulence found that the TLV can form absent a cold-air boundary just by the effect of the mesocyclone updraft lifting streamwise environmental vorticity modified by turbulence in the form of shear-driven rolls (figure 17). Although figure 17 shows a cool-air boundary, simulations with the evaporation of rain artificially suppressed showed similar behavior regarding the TLV. See also figure A3 of Yakota *et al* (2018).

Stipulating that these analyses are technically correct, it is the opinion of the authors that vorticity analysis alone leaves important elements of the TLV dynamics unaccounted for. That is, although one can track the simulated vortex lines and streamlines in simulated TLVs, the physics of how these lines converge toward a common center and turn upward abruptly near ground level requires an analysis of the forces acting on the air parcels possessing vorticity. In the schematic diagrams of figures 14-17, the near-ground flow curves cyclonically towards the center on the horizontal scale of the mesocyclone. This curving can be explained by flow toward the low-pressure mesocyclone center. However, without a downdraft the vertical vorticity so produced would maximize far above the ground (Davies-Jones and Brooks 1993). Although a downdraft is implied by the cold air in figures 14 and 15 it does not indicate a downdraft and figure 17 has only the downdrafts associated with the roll vortices, which are transient features with respect to the supercell updraft and very shallow. We believe it fruitful to look for guidance from simpler axisymmetric models in order to understand the forces at work to produce the trajectories drawn in these figures.

To summarize, while vorticity analysis is essential in understanding many of the features it is generally insufficient for understanding tornado structure influenced by surface friction.

Here are two examples showing that the vorticity analysis (2) by itself is not sufficient to explain tornadogenesis with boundary friction. First consider the axisymmetric model of Davies-Jones (Davies-Jones 2008). Figure 18 (after Davies-Jones 2008) shows the evolution of a storm-scale rotating updraft that produces a TLV. Figure 18(a) represents the supercell by analogy to a Beltrami flow (parallel streamlines and vortex lines, $\boldsymbol{\omega} \times \boldsymbol{u} = 0$; in the absence of buoyancy and friction, it is a steady-state solution of (1). Rain is introduced near r = 0, z = 1 which initially follows a streamline radially outward before falling (figure 18). The negative buoyancy of the falling rain produces a downdraft which transports angular momentum M(=rv) towards the lower boundary which, in turn, initiates the processes leading to the endwall vortex described above (figure 2, lower row) with strong radial inflow near the surface, and an intense upward, swirling jet emerging from the 'corner' region (near the origin). Analysis of the vorticity evolution of air descending into the boundary layer would show frictional generation of horizontal boundary-layer vorticity which, through tilting, accounts for the vorticity of the endwall vortex; vortex lines and streamlines swirl cyclonically along the path much as illustrated in figures 15–17.

The transient behavior of idealized, numerically simulated tornadoes themselves has been shown to be sensitive to significant changes on the scale of the mesocyclone (not in

⁵ This paper appeared online just prior to the submission of the present article. It contains an excellent description of the environmental conditions for tornadic supercells and stages of supercell development leading to the type of tornado that depends crucially on the frictional contact at the lower boundary.

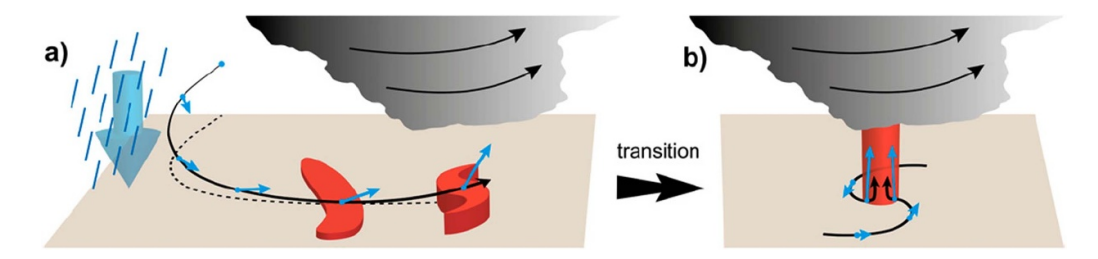


Figure 16. Schematic diagram of the processes leading to tornadogenesis in a supercell simulation with semi-slip boundary conditions. From Fischer and Dahl (2022). © American Meteorological Society. Used with permission.

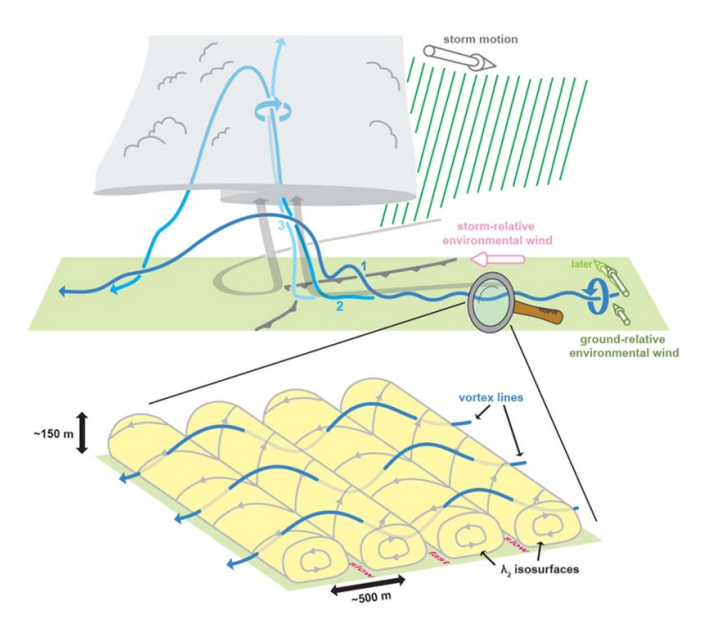


Figure 17. Summary schematic. The mesocyclone is indicated by the cloud, streamlines are in gray and vortex lines are in two shades of blue; the close-up depicts the boundary-layer rolls. From Markowski (2024). © American Meteorological Society. Used with permission.

the synoptic-scale environment), in particular to the relative amount of tangential to radial flow in the corner region of the vortex. If there is a sudden forced decrease in the radial inflow or increase in the swirl, then the vortex may suddenly intensify via 'corner-flow collapse' (Lewellen and Lewellen 2007). This mechanism, of which the Davies-Jones (2008) simulation (figure 18) is an example, has been proposed as way that TLVs may suddenly intensify when the RFD wraps completely around the mesocyclone (occludes), effectively blocking and decreasing low-level radial inflow. This idea has not been tested observationally, applies only to axisymmetric vortices, and buoyancy effects are not considered. Buoyancy effects, however, clearly must be accounted for in real supercells, where mesocyclones are not axisymmetric, at least with respect to buoyancy.

Another, perhaps starker, example comes from considering the boundary layer of a slowly evolving Rankine vortex (inner core in solid-body rotation $v \propto r$ surrounded by a potential vortex $v \propto r^{-1}$; see figure 5(b)) with a no-slip lower boundary condition. Using an axisymmetric numerical

model, Rotunno (Rotunno 2014) simulated the boundary-layer of a slowly evolving Rankine vortex. Figure 19 shows the nondimensional streamfunction and angular momentum; the streamfunction shows a clockwise circulation in the radial-vertical plane. A fluid parcel near r=0.5, z=0.1 enters the boundary layer from above, loses angular momentum and gains radial vorticity $(-r^{-1}\partial\hat{\Gamma}/\partial z)$ through friction, flows radially inward and then upward. In this case the vorticity is exactly zero for the parcel that enters the boundary layer and is only acquired through boundary friction; however, the parcel retains enough angular momentum which, upon flowing to its minimum radius, can produce an intense endwall vortex [see figures 9 and 10 in Rotunno (2014)].

To summarize, in both foregoing examples, there is a circular vortex above the boundary layer with low pressure at the center. A frictional boundary layer inherits the radial pressure gradient from above while reducing the centrifugal forces and thus allowing flow towards lower pressure. Partial conservation of angular momentum in this boundary-layer flow gives rise to the endwall vortex as described above. These examples show that a Lagrangian analysis of vorticity on the parcels that make up the TLV in these cases will arrive at the conclusion that friction accounts for the vorticity of the TLV; however, without understanding the dynamics of the flow (pressure gradients, acceleration, etc) to explain why those air parcels arrive at or near the circulation center, frictional production vorticity as an explanation for the TLV is at best incomplete.

We note here that in these simulations, just as the tornado first appears as an endwall vortex, in rapid-scan mobile Doppler-radar data the tornado vortex signature (TVS, a measurement of the difference between the maximum outbound and inbound Doppler velocities, a proxy for vertical vorticity) in most instances appears first at the lowest elevation angle and builds upward either very rapidly or nearly simultaneously with height (figure 20), though there are some relatively rarer instances where this conclusion might not be apparent (e.g. French *et al* 2013, Houser *et al* 2015, Bluestein *et al* 2019, Houser *et al* 2022; other cases not yet published, H Bluestein; T Greenwood, M S thesis, Greenwood 2021).

The highest azimuthal wind speeds in simulated tornado vortices/tornado-like vortices tend to be at low altitudes (figures 20 and 21). Measuring the wind-speed profiles in the vertical in the tornado boundary layer is very challenging observationally because it is difficult to place reliable instruments in the path of tornadoes and to obtain accurate

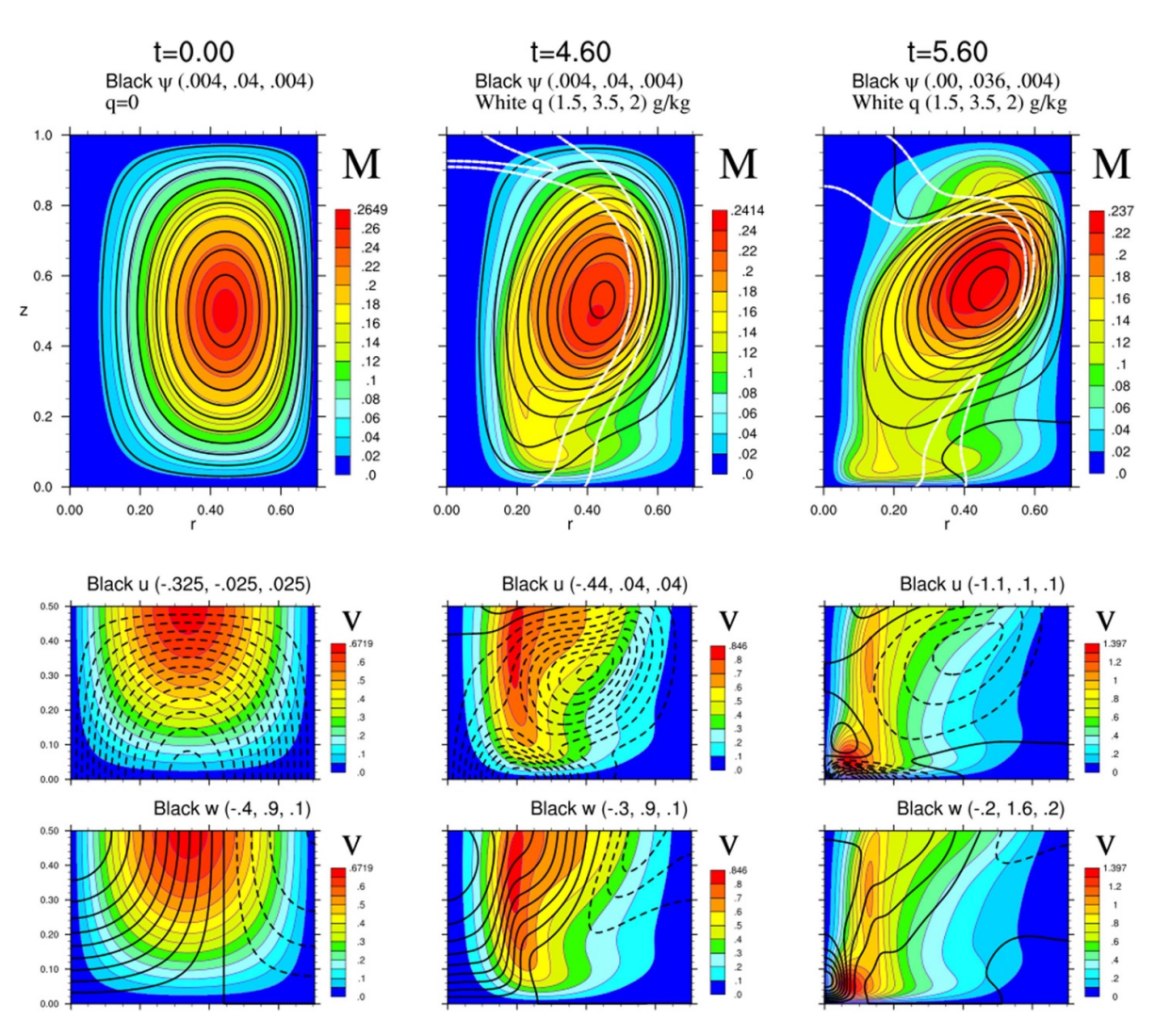


Figure 18. Time sequence of an evolving supercell circulation. First row has the angular momentum M (in color) with the streamfunction in black contours and rainwater mixing ratio in white contours; the second row has the radial velocity in black contours and the third row has the vertical velocity in black contours. The parentheses at the top of each panel give the minimum, maximum and contour interval for the plotted variable; the azimuthal velocity is in color on the second and third rows. Dashed contours indicate negative values. (After Davies-Jones 2008, figure courtesy of R P Davies-Jones).

Doppler-radar measurements near the ground, owing to beam blockage and sidelobe contamination from trees, buildings, etc, debris centrifuging, and beam spreading, among other factors (Snyder and Bluestein 2014). Some of the few good measurements indicate that the strongest winds in a tornado may be at ~25–75 m AGL (Bluestein *et al* 2007, their figure 15) or even as low as~5 m AGL (Kosiba and Wurman 2013, figure 21).

However, there is some visual evidence from falling-tree patterns that the radial-wind component at the ground might be more significant than the tangential velocity, owing to the strongly convergent flow in the surface boundary layer (e.g. Karstens *et al* 2013, their figures 8 and 9; figure 1 in, Snyder and Bluestein 2014). Davies-Jones *et al* (1978) had come to the same conclusion based on observations of litter deposition lines and one-sided mud accumulation on fence posts.

When tornadoes traverse from a region characterized by one surface roughness to another, it is anticipated that the structure of the tornado could change, owing to differences in surface drag. Houser *et al* (2020) has detailed observational attempts to see if differences in topography might be important, with relatively inconclusive results.

A few studies are beginning to simulate tornadic supercells with turbulent boundary layers (Nowotarski *et al* 2015, Markowski 2024), but too few of these studies have been done to establish robust conclusions. Bluestein *et al* (2014) used a combination of mobile Doppler-radar and Doppler lidar observations in an attempt to show turbulent boundary-layer rolls and their relationship to nearby tornadoes. However, the tornadoes were beyond the range of the lidar and it is not clear whether or not the rolls detected were of the same nature as the shallow rolls simulated by Markowski (2024).

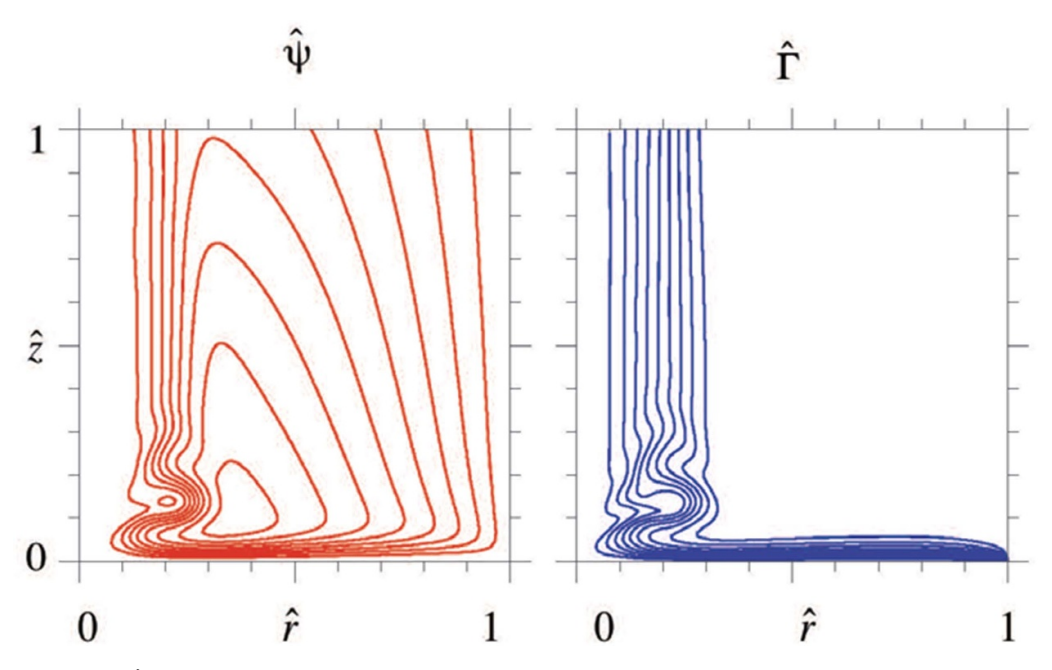


Figure 19. Streamfunction $(\widehat{\psi})$ and angular momentum $(\widehat{\Gamma})$ from a solution for slowly evolving Rankine Vortex with a no-slip condition at the lower surface. Reproduced with permission from Rotunno (2014).

4.5. Sensitivity studies

The sensitivity of tornadogenesis in supercell simulations has been studied from two main angles: sensitivity to the environment (wind profile, thermodynamic instability) and sensitivity to small internal perturbations (turbulence, microphysics of clouds).

4.5.1. Environmental. Using a cloud model (e.g. Bryan and Fritsch, CM1) to simulate supercells, the following studies have investigated the effects of the environmental input parameters on the simulation outputs vis-à-vis the supercell's ability to produce TLVs. Using CM1 Naylor and Gilmore (Naylor and Gilmore 2014) used environmental soundings from an operational forecast model to study the difference between tornadic and nontornadic supercell cases. They found that the CM1 simulations with larger CAPE, smaller CIN and larger SRH in the environment were more likely to produce TLVs. Coffer and Parker (2017, 2018) contrast the differences in the lowest-level wind profiles between nontornadic and tornadic supercells. Figure 22 is their schematic diagram: they find that the most important discriminator between tornadic and nontornadic supercells is the angle between the storm-relative inflow and the shear vector over the lowest 500 m. We note an observation of a low-level hodograph (determined from 'clear-air' return by a mobile Doppler radar) just upstream from a wall cloud in a supercell in Kansas, just minutes before a tornado formed, that the wind direction and strong vertical shear were nearly normal to each other (Bluestein and Pazmany 2000, their figure 7). Parker (2017) shows that upper-level features of the wind profile matter less than previously thought for the TLV potential of a simulated supercell. In an analysis of soundings taken during the VORTEX2 field experiment (Wurman et al 2012), Parker (2014) found that the difference between tornadic and non-tornadic supercells was mostly in lowest several 100 m. These studies show that simulated supercell TLVs can reproduce the observationally determined environmental sensitivity (section 4.2); the analysis of these simulations therefore has the potential to provide a theoretical basis for tornadogenesis.

Sherburn and Parker (Sherburn and Parker 2019) used CM1 to investigate the reasons for TLVs occurring in low-CAPE but high vertical-wind-shear environments. They found that high shear can produce a strong updraft dynamically at low levels (conducive to TLVs) in these environments. Using an ensemble of high-resolution forecasts model, Yokota et al (2018) similarly emphasized the importance of the dynamical interaction between the updraft and shear in favoring TLVs; interestingly, the mechanisms of low-level vorticity/circulation formation were of secondary effect. The importance of the dynamical shear-updraft interactions with respect to TLVs was anticipated in studies of hurricane-associated tornadoes (McCaul and Weisman 1996 MWR). Recently Goldacker and Parker (Goldacker and Parker 2021) simulated a suite of tornadic and non-tornadic supercells based on observed proximity soundings. They found that the tornadic supercell soundings have enhanced SRH over the lowest several hundred meters; this enhancement not only increased the low-level updraft rotation but, perhaps more important, the strength of the low-level updrafts which favors greater vortex stretching below cloud base. Coffer et al (2023) using a similar modeling setup analyzed the trajectories of the parcels composing the strong low-level updraft rotation (the mesocyclone) and found that the vast majority originate from the environment (like trajectory 'A' in figure 6). Coffer et al (2023) draw a distinction between 'low-level' (near cloud base) and 'ground-level' (near or at the surface) arguing that the tilting of environmental vorticity and its effects on the pressure field are

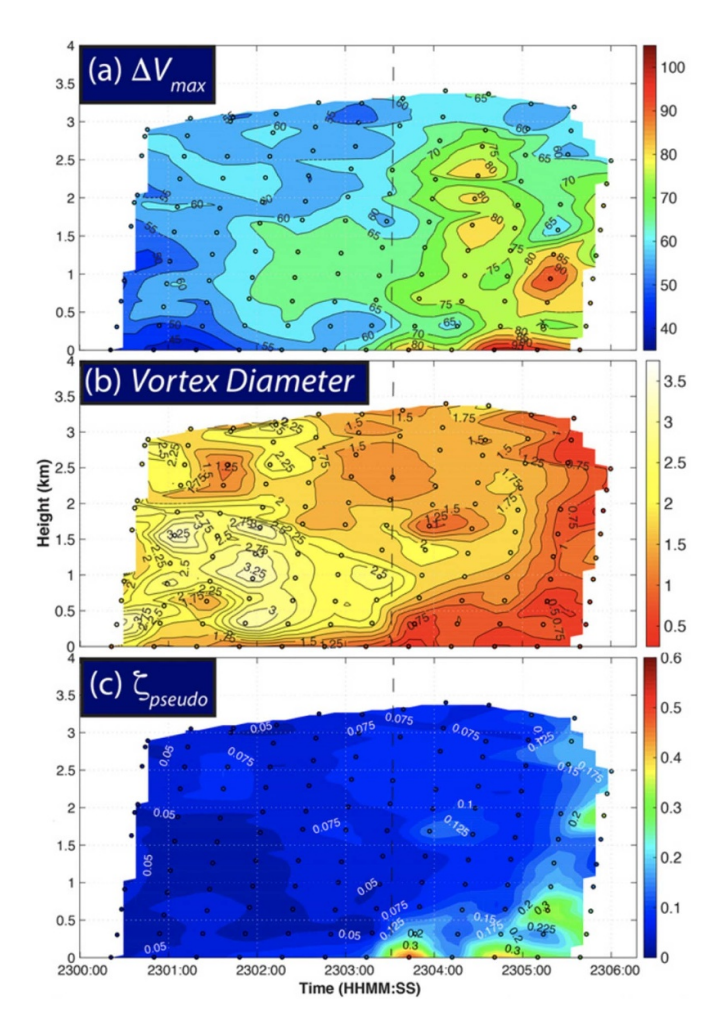


Figure 20. From Bluestein *et al* (2019), their figure 5. ΔV_{max} given in m s⁻¹; vortex diameter given in km; ζ_{pseudo} , twice the Doppler azimuthal shear vorticity, given in s⁻¹; height shown ARL (which is~10 m AGL). (Bluestein *et al* 2019). © American Meteorological Society. Used with permission.

of paramount importance for the tornadic low-level mesocyclone while baroclinic and frictional effects are more precisely referred to as near-ground effects. We have adopted this terminology throughout this report.

Research on potential environmental causes of tornadic supercells is ongoing with notable contributions from Flournoy *et al* (2020) showing that tornado-favorable environments nearer the supercell are much better predictors of TLVs than tornado-favorable environments farther away. Flournoy and Rasmussen (2023) investigated the timing of supercell formation as a function of the strength of the initiating thermal disturbance finding faster evolution with a stronger initial thermal disturbance.

4.5.2. Ensembles, perturbations and forecasting. This research falls under the general topic of atmospheric predictability which distinguishes between practical and intrinsic predictability. Practical predictability is the study of how well (accuracy, timing, etc) a phenomenon (tornadogenesis) can be predicted given current tools (data, finite-resolution models,

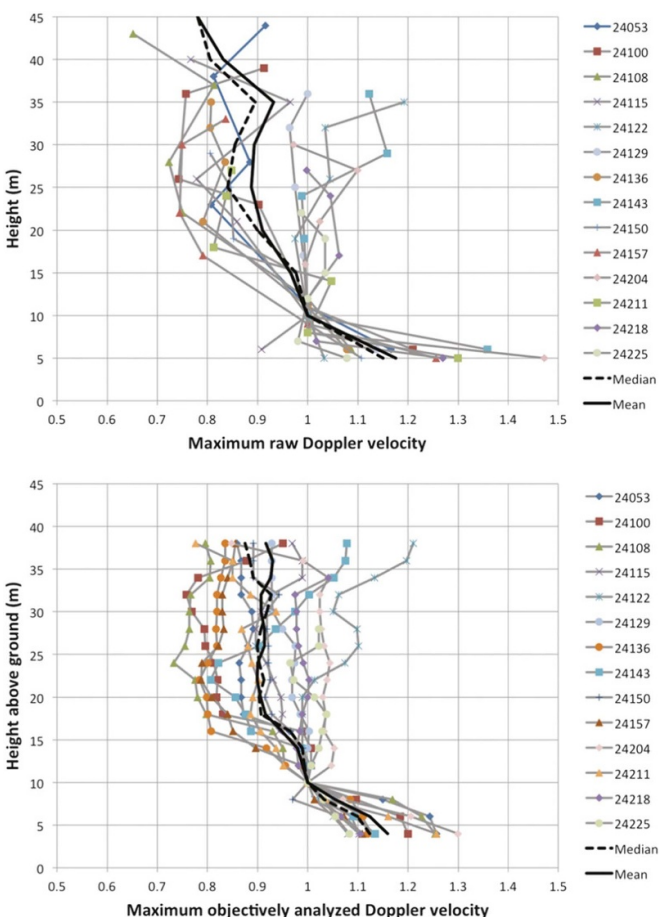


Figure 21. From Kosiba and Wurman (2013), their figure 4. Time labels are shown as HMMss UTC, where H indicates hours. Kosiba and Wurman (2013). © American Meteorological Society. Used with permission.

data-assimilation). Intrinsic predictability is a study of what is theoretically possible with a perfect model which we consider first

Fischer and Dahl (Fischer and Dahl 2020), using CM1 with the MR14 simplified heat source/sink (figure 9), shows that tornadogenesis is very sensitive to the input parameters to the point at which forecasts of which specific supercell among different ones may produce a tornado is not possible. Ensembles of various environmental parameters have been used to study intrinsic predictability. For example, Coffer and Parker (2017) created an ensemble of wind hodographs perturbed around the most favorable hodograph (like that in figure 8). Although differing in detail, each ensemble member produces an intense, long-lived TLV. In a companion experiment using a less-favorable hodograph, about 40% of the ensemble members produced a weak TLV indicating the importance of internal variability. Markowski (Markowski 2020) using a large-eddy simulation (with resolved turbulent eddies) to simulate an ensemble produced by random initial perturbations. Although each ensemble member produced a TLV, they varied considerably in intensity, onset time and duration indicating a limited intrinsic predictability for TLVs. Finally, Parker (2023) created an ensemble of simulations with

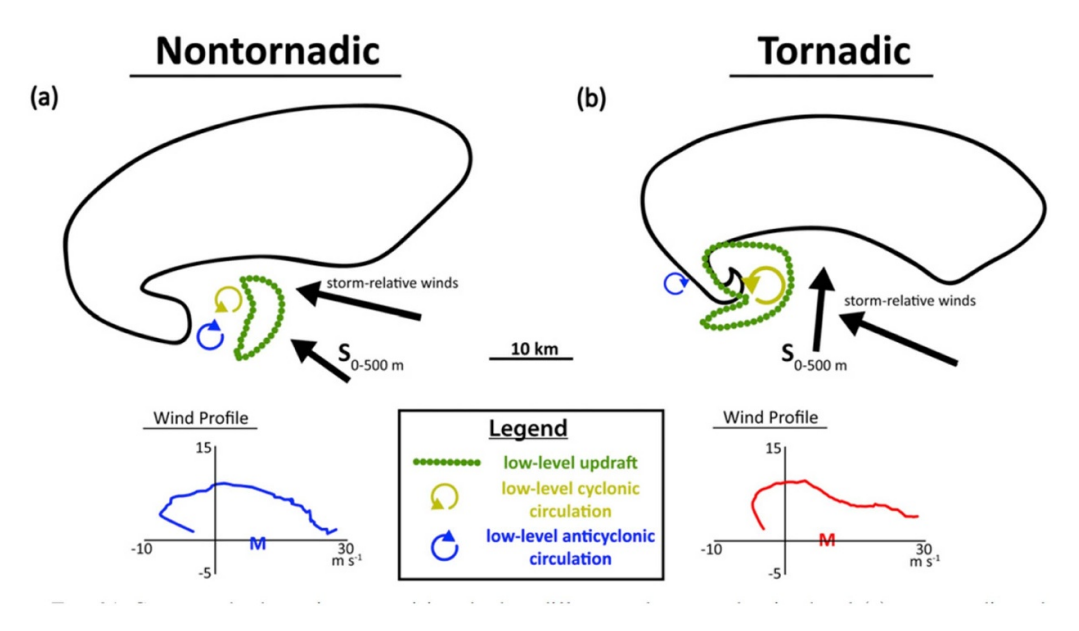


Figure 22. Schematic illustrating the differences in the lowest-level wind profiles between nontornadic and tornadic supercells. From Coffer and Parker (2017). © American Meteorological Society. Used with permission.

a forced updraft and randomly distributed vertical vorticity at low levels. Since the circulation on a level circuit is the area integrated vertical vorticity, each ensemble member has a different low-level circulation. The principal finding is that the details of the vertical vorticity distribution are less important than the associated circulation, with larger circulation (and stronger near-surface convergence) cases leading to stronger TLVs. In a related study Trapp *et al* (2017) examined the relation between hodograph shape, updraft width and tornado intensity in a series of supercell simulations finding that wider storms favored wider more-intense tornadoes. We note that both of these studies using free-slip conditions are strongly analogous to the laboratory studies in which the updraft is forced and the circulation is introduced at low levels (R13, figure 8(a)).

With respect to practical predictability, in an ensemble of high-resolution NWP forecasts for the 20 May 2013 Newcastle–Moore tornado, Snook *et al* (2019) found that 8 of the 10 ensemble members produced intense tornadoes. A greater number of examples are needed to confirm the reliability of the latter finding. The operational Warn on Forecast system (Heinselman *et al* 2023) has shown skill in forecasting significant events (supercells with tornado potential) with several hours of lead time.

5. Future developments

5.1. Theory and modelling

Given the apparent axisymmetry of the tornado and the complex, asymmetric structure of the parent storm, further efforts to understand the physical connections between the two are desirable. For example, an analysis of the forces acting on parcels forming the TLV would presumably highlight the role of the pressure gradient which, in turn, could be related to

the circulation of the parent mesocyclone (Yakota *et al* 2018). Furthermore, identifying the center of an intensifying vortex in the high-resolution supercell simulation could be used to transform the fields to cylindrical coordinates; the azimuthally averaged dynamics could then be compared to that of the axisymmetric models such as those in figures 2, 18 and 19.

The model parameterizations of surface drag, microphysics, turbulence, etc. were all developed for different applications, a critical assessment of these processes in the context of simulating a tornado within a supercell is needed.

Another obvious avenue of future research is the application of machine learning to larger ensembles of high-resolution full-physics supercell simulations over a wider variety of input parameters to distill the essential indicators of tornadic supercells.

5.2. Observations

Centimeter-wave (C and X-band) electronically scanning radars that have polarimetric capability are now being developed which will be able to scan the entire volume of tornadic supercells in just a matter of seconds (Bluestein 2022). These radars will likely reveal with greater accuracy and more detail how tornadoes form in nature and are related to their parent storm and its environment. Radars of this type (rapidscan) that can be built at mm-wavelengths will allow for small antennas having extremely high spatial resolution, necessary to resolve air flow in the tornado boundary layer. However, since attenuation is extreme at these wavelengths, useful data may be collected only when there is relatively little precipitation surrounding the tornado. Polarimetric spectra will be used to separate air motion from debris motion in tornadoes (Bluestein et al 2022, Schneider 2023) and aid in our interpretation of the Doppler-radar observations. Doppler lidar technology will progress to the point that ultra-high spatial resolution and sensitivity can also be attained in the clear-air (without precipitation-size scatterers) tornado boundary layer. Unmanned aircraft systems (UASs) are now being instrumented with video cameras and sensors to detect airflow and thermodynamic properties in the vicinity of storms (e.g. Riganti and Houston 2017) and to document tornado damage swaths (e.g. Wagner *et al* 2021). Markowski *et al* (2018) and Bartos *et al* (2022) have proposed and tested the possibility of using swarms of small, instrumented balloons to acquire detailed thermodynamic measurements in convective storms, which are not otherwise currently possible. UASs in the future may also be fitted with small, relatively lightweight, low-power, phased-array (rapid-scan) mm-wave Doppler radars to probe tornadoes just above the ground.

In the past decade there have been limited, focused, individual and small-team efforts to study tornadic supercells. A new, intensive, larger-scale tornado field program may be justified, however, as revolutionary, new observing systems become available and results from numerical simulation experiments suggest new physical hypotheses to be tested using a large array of such observing systems.

Data availability statement

No new data were created or analysed in this study.

Acknowledgments

Richard Rotunno is supported by the NSF National Center for Atmospheric Research, which is a major facility sponsored by the National Science Foundation under Cooperative Agreement 1852977. Howard B Bluestein is grateful for support from current NSF Grants 1947146 and 2214926 and other earlier NSF Grants. The authors appreciate comments and suggestions on an earlier version of this manuscript by Johannes Dahl, Bob Davies-Jones, Paul Markowski, Matt Parker, Morris Weisman, and Lou Wicker, and discussions with Chris Weiss.

ORCID iDs

Richard Rotunno https://orcid.org/0000-0003-3906-8785 Howard B Bluestein https://orcid.org/0000-0003-1090-2457

References

- Bartos E A, Markowski P M and Richardson Y P 2022
 Three-dimensional thermodynamic observations in supercell thunderstorm from swarms of balloon-borne sondes *Mon. Wea. Rev.* **150** 1689–723
- Bluestein H B 2013 Severe Convective Storms and Tornadoes (Springer) p 456
- Bluestein H B, French M M, Snyder J C and Houser J B 2016 Doppler radar observations of anticyclonic tornadoes in cyclonically rotating, right-moving supercells *Mon. Wea. Rev.* 144 1591–616

- Bluestein H B, Houser J B, French M M, Snyder J C, Emmitt G D, PopStefanija I, Baldi C and Bluth R T 2014 Observations of the boundary layer near tornadoes and in supercells using a mobile, collocated, pulsed Doppler lidar and radar *J. Atmos. Ocean. Technol.* 31 302–25
- Bluestein H B 2022 Observations of tornadoes and their parent supercells using ground-based, mobile Doppler radars *Remote Sensing of Water-Related Hazards (Geophy. Monogr.* vol 271), ed K Y Zhang, Hong and A AghaKouchak (American Geophysical Union, Wiley)
- Bluestein H B and Pazmany A L 2000 Observations of tornadoes and other convective pheonomena with a mobile, 3-mm wavelength, Doppler radar: the spring 1999 field experiment *Bull. Am. Meteor. Soc.* 81 2939–51
- Bluestein H B, Schvartzman D, Yu T-Y, Margraf J, Bodine D J and Cheong B, 2022 Can we advance our understanding of supercell dynamics and microphysics using spectral polarimetry? 17.2A 30th Conf. on Severe Local Storms, (Santa Fe, NM, 28 October) (Amer. Meteor. Soc.)
- Bluestein H B, Snyder J C and Houser J B 2015 A multi-scale overview of the El Reno, Oklahoma tornadic supercell of 31 May 2013 *Wea. Forecast.* 30 525–52
- Bluestein H B, Thiem K J, Snyder J C and Houser J B 2018 The multiple-vortex structure of the El Reno, Oklahoma, tornado on 31 May 2013 *Mon. Wea. Rev.* **146** 2483–502
- Bluestein H B, Thiem K J, Snyder J C and Houser J B 2019 Tornadogenesis and early tornado evolution in the El Reno, Oklahoma, supercell on 31 May 2013 *Mon. Wea. Rev.* 147 2045–66
- Bluestein H B, Weiss C C, French M M, Holthaus E M, Tanamachi R L, Frasier S and Pazmany A L 2007 The structure of tornadoes near Attica, Kansas, on 12 May 2004: high-resolution, mobile, Doppler radar observations *Mon. Wea. Rev.* 135 475–506
- Boyer C H and Dahl J M L 2021 The mechanisms responsible for large near-surface vertical vorticity within simulated supercells and quasi-linear storms *Mon. Wea. Rev.* 148 4281–97
- Browning K A 1964 Airflow and precipitation trajectories within severe local storms which travel to the right of the winds *J. Atmos. Sci.* **21** 634–9
- Coffer B E and Parker M D 2018 Is there a "tipping point" between simulated nontornadic and tornadic supercells in VORTEX2 environments *Mon. Wea. Rev.* **146** 2667–93
- Bunkers M J, Wilson M B, Van Den Broeke M S and Healey D J 2022 Scan-by-scan storm-motion deviations for concurrent tornadic and nontornadic supercells *Wea. Forecast.* 37 749–70
- Coffer B E and Parker M D 2017 Simulated supercells in nontornadic and tornadic VORTEX2 environments *Mon. Wea.* Rev. 145 149–80
- Coffer B E, Parker M D, Dahl J M, Wicker L J and Clark A J 2017 Volatility of tornadogenesis: an ensemble of simulated nontornadic and tornadic supercells in VORTEX2 environments Mon. Wea. Rev. 145 4605–25
- Coffer B E, Parker M D, Peters J M and Wade A R 2023 Supercell low-level mesocyclones: origins of inflow and vorticity *Mon. Wea. Rev.* **151** 2205–32
- Coffer B E, Parker M D, Thompson R L, Smith B T and Jewell R E 2019 Using near-ground storm relative helicity in supercell tornado forecasting *Wea. Forecast.* 34 1417–35
- Coniglio M C and Parker M D 2020 Insights into supercells and their environments from three decades of targeted radiosonde observations *Mon. Wea. Rev.* **148** 4893–915
- Cotton W R, Bryan G H and van den Heever S 2011 Storm and Cloud Dynamics (Academic) p 809
- Dahl J M L 2015 Near-ground rotation in simulated supercells: on the robustness of the baroclinic mechanism *Mon. Wea. Rev.* 143 4929–42

- Dahl J M L 2017 Tilting of horizontal shear vorticity and the development of updraft rotation in supercell thunderstorms J. Atmos. Sci. 74 2997–3019
- Dahl J M L 2021 Centrifugal waves in tornado-like vortices: kelvin's solutions and their applications to multiple-vortex development and vortex breakdown *Mon. Wea. Rev.* 149 3173–216
- Dahl J M L and Fischer J 2023 On the origins of vorticity in a simulated tornado-like vortex *J. Atmos. Sci.* **80** 1361–80
- Dahl J M, Parker M D and Wicker L J 2014 Imported and storm-generated near-ground vertical vorticity in a simulated supercell *J. Atmos. Sci.* **71** 3027–51
- Davies-Jones R P 1984 Streamwise vorticity: the origin of updraft rotation in supercell storms *J. Atmos. Sci.* 41 2991–3006
- Davies-Jones R P 2008 Can a descending rain curtain in a supercell instigate tornadogenesis barotropically? *J. Atmos. Sci.* **65** 2469–97
- Davies-Jones R P 2015 A review of supercell and tornado dynamics *Atmos. Res.* **158–159** 274–91
- Davies-Jones R P 2017 Roles of streamwise and transverse partial-vorticity components in steady inviscid isentropic supercell-like flows *J. Atmos. Sci.* **74** 3021–41
- Davies-Jones R P 2021 Invented forces in supercell models *J. Atmos. Sci.* **78** 2927–39
- Davies-Jones R P 2022 Theory of parcel vorticity evolution in supercell-like flows *J. Atmos. Sci.* **79** 1253–70
- Davies-Jones R P, Burgess D W, Lemon L R and Purcell D 1978 Interpretation of surface marks and debris patterns from the 24 May 1973 Union City, Oklahoma tornado *Mon. Wea. Rev.* 106 12–21
- Davies-Jones R and Brooks H 1993 Mesocyclogenesis from a theoretical perspective *The Tornado: Its Structure, Dynamics, Prediction, and Hazards* ed C Church, D Burgess, C Doswell and R Davies-Jones (American Geophysical Union) pp 105–14 Geophys. Monogr. No. 79
- Davies-Jones R and Markowski P M 2021 Circulation around a constrained curve: an a alternative analysis tool for diagnosing the origins of tornado rotation in numerical supercell simulations *J. Atmos. Sci.* **78** 2895–909
- Esterheld J M and Giuliano D J 2008 Discriminating between tornadic and non-tornadic supercells: a new hodograph technique *Electronic J. Severe Storms Meteor.* **3** 1–50 (available at: https://ejssm.org/archives/)
- Fiedler B H 2017 Axisymmetric tornado simulations with a semi-slip boundary *Fluids* 2 68
- Fischer J and Dahl J M L 2020 The relative importance of updraft and cold pool characteristics in supercell tornadogenesis using highly idealized simulations *J. Atmos. Sci.* 77 4089–107
- Fischer J and Dahl J M L 2022 Transition of near-ground vorticity dynamics during tornadogenesis *J. Atmos. Sci.* **79** 467–83
- Fischer J, Dahl J M, Coffer B E, Houser J L, Markowski P M, Parker M D, Weiss C C and Schueth A 2024 Supercell tornadogenesis: recent progress in our state of understanding *Bull. Am. Meteor. Soc.* **105** E1084–97
- Flournoy M D, Coniglio M C, Rasmussen E N, Furtado J C and Coffer B E 2020 Modes of storm-scale variability and tornado potential in VORTEX2 near- and far-field tornadic environments *Mon. Wea. Rev.* **148** 4185–207
- Flournoy M D and Rasmussen E N 2023 The influence of convection initiation strength on subsequent simulated supercell evolution *Mon. Wea. Rev.* **151** 2179–204
- French M M, Bluestein H B, PopSefanija I and Baldi C A 2013 Reexamining the vertical development of tornadic vortex signatures in supercells *Mon. Wea. Rev.* **141** 4576–601
- Goldacker N A and Parker M D 2021 Low-level updraft intensification in response to environmental wind profiles *J. Atmos. Sci.* **78** 2763–81
- Grams J S, Thompson R L, Snively D V, Prentice J A, Hodges G M and Reames L J 2012 A climatology and comparison of

- parameters for significant tornado events in the United States Wea. Forecast. 27 106–23
- Greenwood T A 2021 Analysis of tornadic supercells using two rapid-scan, mobile doppler radars *M. S. Thesis* University of Oklahoma, Norman p 150 (available at: https://hdl.handle.net/11244/330737)
- Heinselman P *et al* 2023 Warn-on-forecast system: from vision to reality *Wea. Forecast.* **39** 75–95
- Houser J B, McGinnis N, Butler K M, Bluestein H, Snyder J C and French M M 2020 Statistical and empirical relationships between tornado intensity and both topography and land cover using rapid-scan radar observations and a GIS *Mon. Wea. Rev.* 148 4313–38
- Houser J L, Bluestein H B and Snyder J C 2015 Rapid-scan, polarimetric, Doppler radar observations of tornadogenesis and tornado dissipation in a tornadic supercell: The "El Reno, Oklahoma" storm of 24 May 2011 Mon. Wea. Rev. 143 2685–710
- Houser J L, Bluestein H B and Snyder J C 2016 A finescale radar examination of the tornadic debris signature and weak-echo reflectivity band associated with a large, violent tornado *Mon. Wea. Rev.* **144** 4101–30
- Houser J L, Bluestein H B, Thiem K, Snyder J, Reif D and Weinhoff Z 2022 Additional evaluation of the spatiotemporal evolution of rotation during tornadogenesis using rapid-scan mobile radar observations *Mon. Wea. Rev.* **150** 1639–66
- Huang W and Xue M 2023 Subvortices within a numerically simulated tornado: the role of unstable vortex Rossby waves *J. Atmos. Sci.* **80** 2503–29
- Karstens C D, Gallus W A, Lee B D and Finley C A 2013 Analysis of tornado-induced tree fall using aerial photography from the Joplin, Missouri, and Tuscaloosa-Birmingham, Alabama, tornadoes of 2011 *J. Appl. Meteor. Climatol.* **52** 1049–68
- Klemp J B 1987 Dynamics of tornadic thunderstorms *Annu. Rev. Fluid Mech.* **19** 369–402
- Klemp J B, Wilhelmson R and Ray P S 1981 Observed and numerically simulated structure of a mature supercell thunderstorm *J. Atmos. Sci.* **38** 1558–80
- Kosiba K A and Wurman J 2013 The three-dimensional structure and evolution of a tornado boundary layer *Wea. Foreast.* **28** 1552–61
- Lewellen D C and Lewellen W S 2007 Near-surface vortex intensification through corner flow collapse *J. Atmos. Sci.* **64** 2195–209
- Margraf J A 2023 Evolution of the Tornado and Near-Tornado Wind Field of the Selden, Kansas Tornadic Supercell on 24 May 2021 Using a Rapid-Scan, X-Band, Mobile, Doppler Radar *M. S. Thesis* University of Oklahoma, Norman p 227 (available at: https://hdl.handle.net/11244/337059)
- Markowski P M 2020 What is the intrinsic predictability of tornadic supercell thunderstorms? *Mon. Wea. Rev.* **148** 3157–80
- Markowski P M 2024 A new pathway for tornadogenesis exposed by numerical simulations of supercells in turbulent environments *J. Atmos. Sci.* **81** 481–518
- Markowski P M and Richardson Y P 2010 Mesoscale Meteorology in Midlatitude (Wiley) (https://doi.org/10.1002/97804706 82104)
- Markowski P M and Richardson Y P 2014 The influence of environmental low-level shear and cold pools on ornadogenesis: insights from idealized simulations *J. Atmos. Sci.* 71 243–75
- Markowski P M, Richardson Y P, Richardson S J and Petersson A 2018 Aboveground thermodynamic observations in convective storms from balloon borne probes acting as pseudo-Lagrangian drifters *Bull. Am. Meteor. Soc.* 99 711–24
- Markowski P, Richardson Y, Marquis J, Davies-Jones R, Wurman J, Kosiba K, Robinson P, Rasmussen E and Dowell D 2012 The pretornadic phase of the Goshen County, Wyoming, supercell of 5 June 2009 intercepted by VORTEX2. Part II:

- intensification of low-level rotation *Mon. Wea. Rev.* **140** 2916–38
- Marshall J S and Gordon W E 1957 Radiometeorology *Meteorol. Monogr.* **3** 73–113
- Mashiko W 2016 A numerical study of the 6 May 2012 Tsukuba City supercell tornado. Part I: vorticity sources of low-level and midlevel mesocyclones *Mon. Wea. Rev.* **144** 1069–92
- Mashiko W and Niino H 2017 Super high-resolution simulation of the 6 May 2012 Tsukuba supercell tornado: near-surface structure and its evolution *Sci. Online Lett. Atmos.* 13 135–9
- McCaul E W and Weisman M L 1996 Simulations of shallow supercell storms in landfalling hurricane environments *Mon. Wea. Rev.* **124** 408–29
- Naylor J and Gilmore M S 2014 Vorticity evolution leading to tornadogenesis and tornadogenesis failure in simulated supercells *J. Atmos. Sci.* **71** 1201–17
- Nolan D S, Dahl N A, Bryan G H and Rotunno R 2017 Tornado vortex structure, intensity, and surface wind gusts in large-eddy simulations with fully developed turbulence *J. Atmos. Sci.* **74** 1573–97
- Nowotarski C J and Jensen A A 2013 Classifying proximity soundings with self-organizing maps toward improving supercell and tornado forecasting *Wea. Forecast.* **28** 783–801
- Nowotarski C J and Jones E A 2018 Multivariate self-organizing map approach to classifying supercell tornado environments using near-storm, low-level wind and thermodynamic profiles *Wea. Forecast.* 33 661–70
- Nowotarski C J, Markowski P M, Richardson Y P and Bryan G H 2015 Supercell Low-Level Mesocyclones in Simulations with a Sheared Convective Boundary Layer *Mon. Weather Rev.* 143 272–97
- Orf L, Wilhelmson R, Lee B, Finley C and Houston A 2017 Evolution of a long-track violent tornado within a simulated supercell *Bull. Am. Meteor. Soc.* **98** 45–68
- Parker M D 2012 Impacts of lapse rates on low-level rotation in idealized storms *J. Atmos. Sci.* **69** 538–59
- Parker M D 2014 Composite VORTEX2 supercell environments from near-storm soundings *Mon. Wea. Rev.* **142** 508–29
- Parker M D 2017 How much does "backing aloft" actually impact a supercell? Wea. Forecast. 31 1937–57
- Parker M D 2023 How well must surface vorticity be organized for tornadogenesis? *J. Atmos. Sci.* **80** 1433–48
- Parker M D and Dahl J M L 2015 Production of near-surface vertical vorticity by idealized downdrafts *Mon. Wea. Rev.* **143** 2795–816
- Riganti C J and Houston A L 2017 Rear-flank outflow dynamics and thermodynamics in the 10 Juen 2010 Last Chance, Colorado, supercell Mon. Wea. Rev. 145 2487–504
- Roberts B, Xue M, Schenkman A D and Dawson D T 2016 The role of surface drag in tornadogenesis within an idealized supercell simulation *J. Atmos. Sci.* **73** 3371–95
- Roberts B, Xue M, Schenkman A D and Dawson D T 2020 The effect of surface drag strength on mesocyclone intensification and tornadogenesis in idealized supercell simulations *J. Atmos. Sci.* 77 1699–721
- Rotunno R 2013 The fluid dynamics of tornadoes *Annu. Rev. Fluid Mech.* **45** 59–84
- Rotunno R 2014 Secondary circulations in rotating-flow boundary layers *Aust. Meteorol. Oceanogr. J.* **64** 27–35
- Rotunno R, Bryan G H, Nolan D S and Dahl N A 2016 Axisymmetric tornado simulations at high Reynolds number *J. Atmos. Sci.* **73** 3843–53

- Rotunno R and Klemp J B 1985 On the rotation and propagation of simulated supercell thunderstorms *J. Atmos. Sci.* **42** 271–92
- Rotunno R, Markowski P M and Bryan G H 2017 "Near-ground" vertical vorticity in supercell thunderstorm models *J. Atmos. Sci.* **74** 1757–66
- Schenkman A D, Xue M and Hu M 2014 Tornadogenesis in a high-resolution simulation of the 8 May 2003 Oklahoma City supercell *J. Atmos. Sci.* **71** 130–54
- Schneider M 2023 A novel technique to correct debris centrifuging bias in Doppler velocity measurements of tornadoes 40th Conf. on Radar Meteorology (Amer. Meteor. Soc.) p 15B
- Schueth A, Weiss C and Dahl J M L 2021 Comparing observations and simulations of the streamwise vorticity current and the forward-flank convergence boundary in a supercell storm *Mon. Wea. Rev.* **149** 1651–71
- Sherburn K D and Parker M D 2014 Climatology and ingredients of significant severe convection in high-shear, low-CAPE environments J. Atmos. Sci. 29 854–77
- Sherburn K D and Parker M D 2019 The development of severe vortices within simulated high-shear, low-CAPE convection *Mon. Wea. Rev.* 147 2189–216
- Snook N, Xue M and Jung Y 2019 Tornado-resolving ensemble and probabilistic predictions of the 20 May 2013 Newcastle–Moore EF5 tornado *Mon. Wea. Rev.* **147** 1215–35
- Snyder J C and Bluestein H B 2014 Some considerations for the use of high-resolution mobile radar data in tornado intensity determination *Wea. Forecast.* **29** 799–827
- Tao T and Tamura T 2020 Numerical study of the 6 May 2012 Tsukuba supercell tornado: vorticity sources responsible for tornadogenesis Mon. Wea. Rev. 148 1205–28
- Thompson R L, Edwards R, Hart J A, Elmore K L and Markowski P M 2004 Close proximity soundings within supercell environments obtained from the rapid update cycle *Wea. Forecast.* **18** 1243–61
- Trapp R J, Marion G R and Nesbitt S W 2017 The regulation of tornado intensity by updraft width *J. Atmos. Sci.* **74** 4199–210
- Wade A R, Coniglio M C and Ziegler C L 2018 Comparison of near- and far-field supercell inflow environments using radiosonde observations *Mon. Wea. Rev.* **146** 2403–15
- Wagner M A, Doe R K, Wang C, Rasmussen E, Coniglio M C, Elmore K L, Balling R C Jr and Cerveny R S 2021 High-resolution observations of microscale influences on a tornado track using unpiloted aerial systems (UAS) *Mon. Wea. Rev.* 149 2819–34
- Wakimoto R M, Wienhoff Z, Reif D, Bluestein H B and Lewellen D C 2022 The Dodge City tornadoes on 24 May 2016: understanding cycloidal marks in surface damage tracks and further analysis of the debris cloud *Mon. Wea. Rev.* **150** 1233–46
- Wang A, Pan Y, Bryan G H and Markowski P M 2023 Modeling near-surface turbulence in large-eddy simulations of a tornado *Mon. Wea. Rev.* **151** 1587–607
- Wurman J, Dowell D, Richardson Y, Markowski P, Rasmussen E, Burgess D, Wicker L and Bluestein H B 2012 The second verification of the origins of rotation in tornadoes experiment: VORTEX2 Bull. Am. Meteorol. Soc. 93 1147–1170.
- Wyngaard J C 2004 Towards numerical modeling in the "terra incognita *J. Atmos. Sci.* **61** 1816–26
- Yakota S, Niino H, Seko H, Kunii M and Yamauchi H 2018 Important factors for tornadogenesis as revealed by high-resolution ensemble forecasts of the Tsukuba supercell tornado of 6 May 2012 in Japan *Mon. Wea. Rev.* 146 1109–32